Seismic structure of the Eastern European crust and upper mantle from probabilistic ambient noise tomography

Laura Petrescu [a,*], Felix Borleanu [a], Emanuel Kästle [b], Randell Stephenson [c], Anica Plăcintă [a], Oleksandr Ivanovich Liashchuk [d]

[a] National Institute for Earth Physics, Măgurele, Romania
[b] Freie Universität Berlin, Institute of Geological Sciences, Berlin, Germany
[c] University of Aberdeen, School of Geosciences, Aberdeen, United Kingdom
[d] Main Center of the Special Monitoring, State Space Agency of Ukraine, Kyiv, Ukraine

ABSTRACT

The Eastern European lithosphere is a natural laboratory to study continental formation and evolution through time, comprising Archean continental remnants, Proterozoic rifts and belts, and younger accreted terranes. We investigate the seismic structure of the East European Craton (EEC) crust and uppermost mantle, and the transition from Precambrian to Phanerozoic Europe across the Trans European Suture Zone (TESZ) using probabilistic transdimensional ambient noise tomography. We cross-correlate noise recorded at broadband seismic stations from Eastern, Northern, and Central Europe, remove earthquake signals using continuous wavelet transform, and extract Rayleigh wave phase velocity dispersion curves. We invert these for the highest resolution shear wave velocity model of the Eastern European lithosphere to date, using Markov chain Monte Carlo Bayesian inversion. Our shear wave velocity model exhibits spatial correlation with major tectonic units and bears similarities with active seismic survey profiles in terms of seismic velocity patterns and main discontinuities. The crust thickens across the TESZ boundary and the mantle is seismically faster than beneath younger terranes, consistent with a less dense Precambrian lithosphere in the EEC. The crust and lithosphere beneath the Pannonian region is hyper-extended but the adjacent Transylvanian basin crust shows significant heterogeneity. The Precambrian building blocks of the EEC exhibit contrasting seismic fabrics. The Baltic orogens of Fennoscandia are underlain by uniform crust with a flat Moho, while Sarmatia shows alternating high and low velocity layers and a regional south-dipping crustal boundary from beneath the Ukrainian Shield towards the Crimean Peninsula. The last observation supports a geodynamic style driven by horizontal rather than vertical tectonics, with fundamental implications for the formation and evolution of early continents.

© 2023 The Authors. Published by Elsevier B.V. on behalf of International Association for Gondwana Research. This is an open access article under the CC BY-NC-ND license (http://creativecommons.org/licenses/by-nc-nd/4.0/).

1. Background

The Precambrian nuclei of continents, such as the East European Craton, display anomalously thick present-day lithosphere and distinct crustal structure and composition. These continental nuclei were consolidated and assembled over a long period of Earth history, from the Archean when the Earth was likely too hot to sustain modern plate tectonics through a transition into the Paleoproterozoic, when accretionary processes similar to those observed in the Phanerozoic were initiated (e.g. Stern, 2005; Hamilton, 2011). The Precambrian lithosphere displays a spectrum of different tectonic styles that have been, in turn, overprinted by those that are representative of a younger Earth. Secular changes in mantle properties might have facilitated continental crustal growth in either a vertical or a lateral sense, depending on the dominant geodynamic process that operated at different times (e.g. Durrheim and Mooney, 1991) generating distinct crustal structures, compositions and deformation fabrics (e.g. Zegers and Van Keken, 2001). For example, Archean crust may be thinner and have a more felsic composition than Proterozoic crust (e.g. Petrescu et al., 2016), which could reflect secular cooling of Earth's mantle (Yuan, 2015). Plate tectonics whose onset time has not been precisely determined (Korenaga, 2013) likely played a fundamental role in changing the style of crustal growth within and around the Earth's surviving cratons.

* Corresponding author.
E-mail address: laura.petrescu@infp.ro (L. Petrescu).

The European continent evolved throughout several cycles of continental break-up and accretion at the margins of the East European Craton (Fig. 1a, Nikishin et al., 1996; Bogdanova et al., 2008; Ustaszewski et al., 2008; Mints, 2015) at present bordered by the Ural Mountains in the east (e.g. Stephenson et al., 2006), the Trans-European Suture Zone and the Carpathian Mountains in the west (Pharaoh et al., 2006) and the Alpine-Tethys belt to the south (Gee and Stephenson, 2006). The EEC is a thick and seismically fast craton comprising several Archean cores and Proterozoic belts and paleorifts (Bogdanova et al., 1996; Claesson et al., 2006; Stephenson et al., 2021). Investigating the crustal structure of these cores and how they transition into younger continental crust can offer fundamental clues on the Earth's evolution through geological history, the onset of plate tectonics or the kind of processes that regulate crustal growth (e.g. Durrheim and Mooney, 1991; Mints, 2018).

We investigate the crustal and uppermost mantle seismic structure using ambient seismic noise and the most recent noise processing tools and methods, using data from broadband permanent and temporary seismic stations that operated in Central, Northern and Eastern Europe between 1999 and 2020 (Fig. 1b). We cross-correlate ambient seismic noise records and stack these to obtain virtual impulse response functions between pairs of stations. We then extract Rayleigh wave phase velocity dispersion curves from each inter-station virtual Green's function (Kästle et al., 2016) and combine them to determine the isotropic phase velocity and azimuthal anisotropy at discrete periods (e.g. Darbyshire and Lebedev, 2009). We then invert these data using a transdimensional Hierarchical Bayesian algorithm (Bodin et al., 2012) to obtain a 3D shear wave velocity model of the East European Craton, the Trans-European Suture Zone, and the adjacent accreted tectonic microplates down to ∼60 km depth. Our new results provide the first 3D crustal seismic images of an area that has not been explored before at such high resolution and wide spatial extent. Additionally, azimuthal anisotropy can offer fundamental clues on deformation patterns frozen in the crust due to past tectonic events (e.g. Wüstefeld et al., 2010).

2. Tectonic setting

The East European Craton, which approximates the proto-continent known as Baltica (e.g. Bogdanova et al., 2008), is a tectonic collage of three Precambrian continental nuclei with
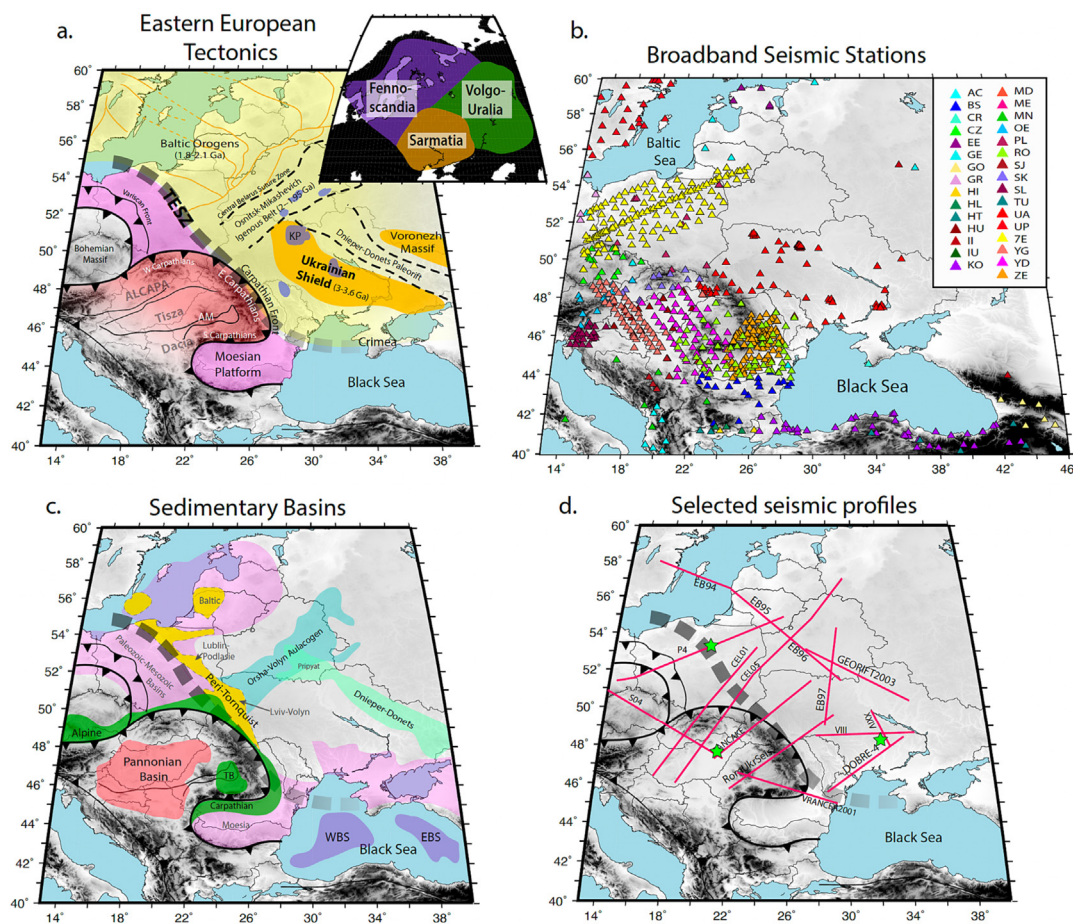

Fig. 1. a. Map of central, eastern, and part of northern europe showing the major geological boundaries and tectonic setting. the yellow area marks the east european craton. blue patches are proterozoic anorthosite complexes, including the Korosten Pluton (KP). The pink areas are Avalonian blocks presumably sutured to the EEC. The red area marks the Carpathian embayment with Phanerozoic microplates hosting the Pannonian and Transylvanian Basin and the Apuseni Mountains (AM). The thick dashed black line outlines the Teisseyre–Tornquist Line. Its route is less certain beneath the Carpathians. Inset shows the micro-continents forming the East European Craton. b. Map showing all the broadband seismic stations whose data were analysed in this study, colored according to their seismic network. The legend shows network codes and acronyms, which can be found on http://orfeus-eu.org (last accessed May 2022) and https://www.fdsn.org/networks (last accessed May 2022). c. Approximate boundaries of the main sedimentary basins of Central, Northern, and Eastern Europe after Nelskamp (2017). the European Permian Basin and Paleozoic deposits (pink), the Peri- Tornquist Basins (yellow), the Pannonian Basin (red), Carpathian foreland deposits and Transylvanian Basin (TB, green), the Western and Eastern Black Sea Basins (WBS and EBS, purple), the Pripyat-Dnieper-Donets basins (light green), and the Orsha-Volyn Aulacogen (blue), part of the Central Russian Rift System. d. Selected seismic survey lines crossing the main geological boundaries in Eastern Europe. Green stars mark the location of 1D inversion examples in Fig. 3. (For interpretation of the references to colour in this figure legend, the reader is referred to the web version of this article.)

Archean cores (Mints, 2015) separated by Proterozoic belts and paleorifts: Fennoscandia, Sarmatia, and Volgo-Uralia (Fig. 1a). Sarmatia, which is of Archean-Paleoproterozoic age, is exposed in the Ukrainian Shield and Voronezh Massif. Sarmatia and Fennoscandia are sutured along the Central Belarus Suture Zone and the 2–1.95 Ga Osnitsk-Mikashevich Igneous Belt (OMIB, Bogdanova et al., 2006), which subsequently became the site of extension and rifting forming the Central Russian Rift System (Gorbatschev and Bogdanova, 1993; Krzemińska et al., 2022). Northwest of the Central Belarus Suture Zone, Fennoscandia comprises a series of Baltic orogenic belts formed between 2.1 Ga and 1.9 Ga that are partly submerged beneath the Baltic Sea and can be traced onto the Scandinavian Peninsula (Bogdanova et al., 2015). The EEC was involved in multiple supercontinent cycles and survived the impacts of several mantle plumes. Sarmatia records magmatic traces of at least two inferred mantle plumes of Precambrian age (Shumlyanskyy et al., 2016) and is scarred by large igneous intrusions such as the Korosten Pluton, a 1.8–1.7 Ga large igneous complex that may extend down to ∼20 km (Thybo et al., 2003). The break-up of the Neoproterozoic supercontinent Rodinia led to the formation of the western boundary of Baltica at the TESZ inducing widespread flood basalt volcanism, remnants of which are preserved in the Volyn large igneous province (Krzemińska et al., 2022; Shumlyanskyy et al., 2007), spanning ∼200,000 km^2 across western Ukraine, eastern Poland, and south-western Belarus, and cross-cutting the OMIB (Fig. 1a). The Pripyat- Dnieper-Donets graben, a paleorift hosting Paleozoic-aged basins (Stephenson et al., 2021), cross-cuts Sarmatia and superimposes on the OMIB, and may be the consequence of another mantle plume that thermochemically eroded the cratonic lithosphere (Wilson and Lyashkevich, 1996).

The western margin of Baltica acted as a buffer zone for multiple continental collisions, remnants of which are collectively termed the Trans-European Suture Zone (TESZ, Pharaoh, 1999; Grad et al., 2002). The TESZ is the most important geological boundary zone in Europe (Fig. 1), extending from the Baltic to the Black Sea beneath the Carpathians (Borleanu et al., 2021). The TESZ separates Precambrian aged terranes of the EEC from younger microplates and oceanic tracts progressively to its western margin. Several orogenic fronts advanced towards the craton, but deformation typically terminated parallel to the TESZ: the Caledonian front marks the collision between Baltica (present-day EEC) and the Avalonia paleo-continent roughly 490–390 million years ago, resulting in the accretion of Avalonia-affined terranes (e.g. Oczlon et al., 2007) and the development of the *peri*-Tornquist sedimentary Basins (Poprawa, 2019) on the passive margin of Baltica (Fig. 1c). The Variscan Front (Fig. 1a) marks the collision between the extended Baltican margin with Gondwana approximately 370–290 million years ago, contributing to the growth of the European continent westwards and southwards (Behr et al., 1984). The Alpine-Carpathian Front marks the limit of Neogene deformation due to the northward migration of Africa and its Adriatic promontory, resulting in the accretion of the Alcapa, Tisza, and Dacia terranes (Fig. 1a), as well as several neo-Tethys oceanic tracts to the southwestern margin of the EEC (Ustaszewski et al., 2008). Finally, the hyper-extended Pannonian Basin (Horváth et al., 2006) and the Transylvanian Basin (Fig. 1c) evolved in the back-arc region relative to the Carpathians, subsequently experiencing sporadic post-collisional volcanism over the last 12 million years (e.g. Seghedi et al., 2004; Bracco Gartner and McKenzie, 2020).

The structure of the EEC crust and upper mantle, the TESZ and the younger terranes to the west have been investigated with a plethora of seismic imaging tools, including seismic tomography (e.g. Zielhuis and Nolet, 1994; Zhu et al., 2012), receiver functions (e.g. Knapmeyer-Endrun et al., 2013; Kalmár et al., 2023) and active seismic techniques such as modern deep seismic sounding and wide angle reflection and refraction seismic surveys (Fig. 1d): BABEL (BABEL Working Group, 1993), POLONAISE97 (P4, e.g. Guterch et al., 1999; Grad et al., 2002), EUROBRIDGE'94-'97 (EB'97, e.g. EUROBRIDGE Seismic Working Group, 1999; Yliniemi et al., 2001), CELEBRATION2000 (CEL01, CEL05, e.g. Grad et al., 2006; ÅLSroda et al., 2006), VRANCEA'99-'01 (Hauser et al., 2001, 2007), PANCAKE (Starostenko et al., 2013), and RomUkrSeis (Starostenko et al., 2020). Seismic surveys, however, have the limitation of a 2D view of local-sized cross-sections and may not be able to capture the complexities of structural heterogeneity and deformation that shaped the EEC margin. A large-scale 3D seismic tomography of the crust and upper mantle can provide significant added-value to reveal the nature and evolution of the European continent through time.

3. Data and methods

To investigate the structure of the East European Craton and the transition from Precambrian crust and lithospheric mantle into Phanerozoic terranes accreted to its western flanks, we use the most recently developed ambient seismic noise tomography techniques. Ambient noise tomography (ANT) has been an increasingly popular seismic imaging tool in the last few decades thanks to the widespread availability of continuous seismic records from dense arrays and an increase in computing power. ANT relies on the principle that cross-correlating ambient noise recorded at pairs of seismic receivers yields impulse response functions of the Earth's structure, known as empirical Green's functions. These are similar to real seismograms and include virtual Rayleigh waves, whose properties can be used to infer information on subsurface structures (e.g. Ritzwoller and Levshin, 1998). ANT removes the need to record unevenly distributed earthquakes, offering the possibility to improve azimuthal ray coverage and, implicitly, resolution, by turning stations into virtual sources (Curtis et al., 2006). Previous models of the crust and lithosphere in the EEC based on earthquake data (e.g. Bijwaard and Spakman, 2000; Zhu et al., 2012) suffer from this azimuthal coverage deficiency which automatically lowers model resolution and impedes accurate estimation of seismic velocities and their directional variation, a crucial additional parameter that can help constrain past deformational features and/or active mantle flow (e.g. Petrescu et al., 2022).

Bensen et al. (2007) developed a reference procedure for processing and analysing ambient noise data, which was progressively modified and improved (e.g. Yang et al., 2020). Here we follow the general procedure of Bensen et al. (2007) with several modifications. The ANT is done in multiple steps: 1. Continuous ground motion cross-correlation and stacking; 2. Extraction of interstation Rayleigh wave dispersion curves; 3. Estimation of phase velocity lateral distribution in frequency domain (e.g. Darbyshire and Lebedev, 2009; Petrescu et al., 2017); 4. Inversion of phase velocity maps into 3D shear wave velocity tomography (e.g. Petrescu et al., 2022). Recently developed processing tools and the wealth of both permanent and temporary seismic networks in Eastern Europe (Fig. 1) provide an excellent opportunity to illuminate crustal and uppermost mantle structure of a complexly evolved continent using ambient noise.

3.1. Ambient noise processing

We use continuous noise records from 1477 broadband permanent and temporary seismic stations located throughout Central, Northern and Eastern Europe (Fig. 1), out of which 338 stations belong to temporary networks including the CALIXTO seismic experiment in 1999 (Martin et al., 2005), the Carpathians Basins

Project which operated in 2005–2007 (CBP, Dando et al., 2011), the PASSEQ experiment from 2006 to 2008 (Wilde-Piorko et al., 2008), and the South Carpathians Project from 2009 to 2011 (SCP, Ren et al., 2012). We downloaded available data from permanent stations from national seismic networks that overlap with the period range of the temporary deployments and from 2013 to 2020, archived at EIDA (European Integrated Data Archive) and IRIS DMC (Incorporated Research Institutions for Seismology Data Management Center). Data from seismic stations in Ukraine were provided by the Main Centre of Special Monitoring State Space Agency of Ukraine for the year 2020.

Continuous vertical-component ground motion records are downloaded in 24-hour long traces, resampled to 5 sps (0.2 s time increment) and visually inspected to ensure the data do not exhibit anomalous notches or patterns due to instrument failure. We then cut continuous ambient seismic noise data in hour-long seismograms, we apply spectral whitening with a waterlevel value of 60 dB relative to the amplitude of the spectrum, cross-correlate and stack, obtaining inter-station empirical Green's functions. Data with gaps>10 s are discarded and smaller gaps are zero-padded. Prior to cross-correlation we remove the instrument response, the mean and the trend, and apply a Butterworth filter with corner frequencies between 0.003 Hz and 2.4 Hz. To eliminate high amplitude transients that disturb the ambient noise field, such as earthquakes or anomalous pulses, we use a recently developed designaling algorithm based on the Continuous Wavelet Transform (CWT, Yang et al., 2020). At this point, data are again visually inspected to ensure the CWT successfully extracted background noise. Seismograms with residual signals are discarded. The CWT is also applied in reverse to de-noise the final cross-correlation traces, resulting in high signal-to-noise ratio waveforms with well-defined Rayleigh wave packets (Fig. 2). Finally, from the available simultaneously operating station pairs, we obtained 75,012 empirical Green's functions for inter-station distances between 32 km and 2901 km. Possible methods to reconstruct Green's functions between stations that did not operate at the same time might include the correlation of coda-correlations (e.g. Chen et al., 2023).

3.2. Surface wave dispersion

We extract Rayleigh wave phase velocity dispersion curves using an automatic phase-picking algorithm (Fig. 2), which assumes that vertical cross-correlograms take the form of Bessel functions (Kästle et al., 2016; Magrini et al., 2022). In this method, consecutive null values of the cross-correlation spectrum yield direct measurements of phase velocity-frequency dispersion curves subject to several stabilising criteria. These include enforcing a maximum departure from a reference model to avoid irregularities, picking consecutive zero-spectrum phase velocities $c(\omega)$ for frequency steps $\sim \pi$ and ensuring the associated Bessel function has the same polarity as $\Re(c(\omega))$. This method has been successfully applied in ambient noise tomography (Petrescu et al., 2022) and yielded 21,074 high-quality dispersion curves between stations as far apart as 2870 km. The number of dispersion curves is significantly lower than the Greens' functions set, due to the strict quality control criteria applied during the automatic dispersion analysis.

We associate an elliptical-shaped kernel with each zero crossing that has a cosine decay of the intensity/weight from 1 in its center to 0 at the border of the ellipse (Kästle et al., 2022). The kernel width and height are user-controlled in units relative to the spacing between adjacent zero crossings. By summing the overlapping kernel intensities/weights from all zero crossings, a final heatmap is obtained from which the dispersion curve is picked (Fig. 2c and d). The dispersion curve picking algorithm starts at low frequencies and successively picks phase velocities until one or several of the stopping criteria are met. These criteria are sudden changes in the slope, a slope that deviates too much from the reference curve or missing picks due to missing zero crossings. In Fig. 2d, this can be seen around 0.1 Hz where the red dispersion picks stop. The heatmap in the background is calculated in an iterative manner, so that it is always ~0.025 Hz ahead of the last pick. When the picking algorithm stops, the heatmap is also not calculated further for higher frequencies.

3.3. Rayleigh wave phase velocity tomography

The Rayleigh wave dispersion curves are combined into a damped and gridded phase velocity tomography in a discrete period interval from 4 s to 50 s. At these periods, Rayleigh waves sample predominantly crustal and uppermost mantle depths. Each grid cell is defined by its total phase velocity anomaly, which is deconstructed via Fourier expansion into isotropic and azimuthally anisotropic terms:

$$\delta C = \delta C_{iso} + A_{2\psi} cos(2\psi) + B_{2\psi} sin(2\psi) + A_{4\psi} cos(4\psi) + B_{4\psi} sin(4\psi)$$

(1)

where ψ is the horizontal wave-number azimuth and δC is the total phase velocity anomaly at the considered grid knot. This equation is similar to a Fourier expansion (Deschamps et al., 2008) and the azimuthal anisotropy amplitude and direction are a linear combination of the equation's coefficients A and B (e.g. Petrescu et al., 2017). These coefficients are estimated using a damped LSQR procedure (Paige and Saunders, 1982; Darbyshire and Lebedev, 2009). This type of geophysical inversion algorithm does not yield covariance matrices. Deschamps et al. (2008) adopted a Monte Carlo approach to estimate standard deviation errors from a dataset of 60 paths, obtaining values between 8 and 12 m/s which are insignificant compared to mapped phase velocity heterogeneities. Considering our dataset is much larger, we would not expect the error on our dispersion curve data to be higher.

The model is parametrized on a triangular grid using spherical splines (Wang and Dahlen, 1995) covering the Earth's surface with an approximately equal interknot spacing of 60 km. This is similar to previous surface wave tomography models using interknot spacings between 50 km and 100 km depending on area and ray coverage (e.g. Li et al., 2010; Legendre et al., 2012, 2015; Shen et al., 2016). The 3-D perturbations of phase velocities are estimated at each grid knot and interpolated on a denser triangular grid, with knot spacing about a third of the original model grid. The period interval for which dispersion functions are estimated vary, resulting in different ray path coverage at each period. Consequently, the size of the grid is different for each period. A good coverage such as that for the 30 s period results in a grid of 1180 knots, while for the 10 s period, the grid size is under 1000 knots.

Our preferred damping and smoothing parameter combination is based on trade-off curves between model roughness and the ability to explain the observed data, defined through variance reduction (Figure S2 in the Supplementary Material). This LSQR procedure requires two types of damping. The primary type of damping (or lateral smoothing) minimizes the difference between a grid point and the average over the surrounding points. The second type of damping penalizes the second spatial derivative of each term. Increased damping and smoothing parameters thus decrease anomaly values and lateral gradients, but also decrease data fit. To find the damping parameters, we plot trade-off curves between smoothing and variance, and roughness versus variance, respectively, for each period, for very low damping parameters, while keeping the anisotropic term damping values constant. The knee of the resulting curves and their approximate intersection yields optimum smoothing values. We proceed similarly for the
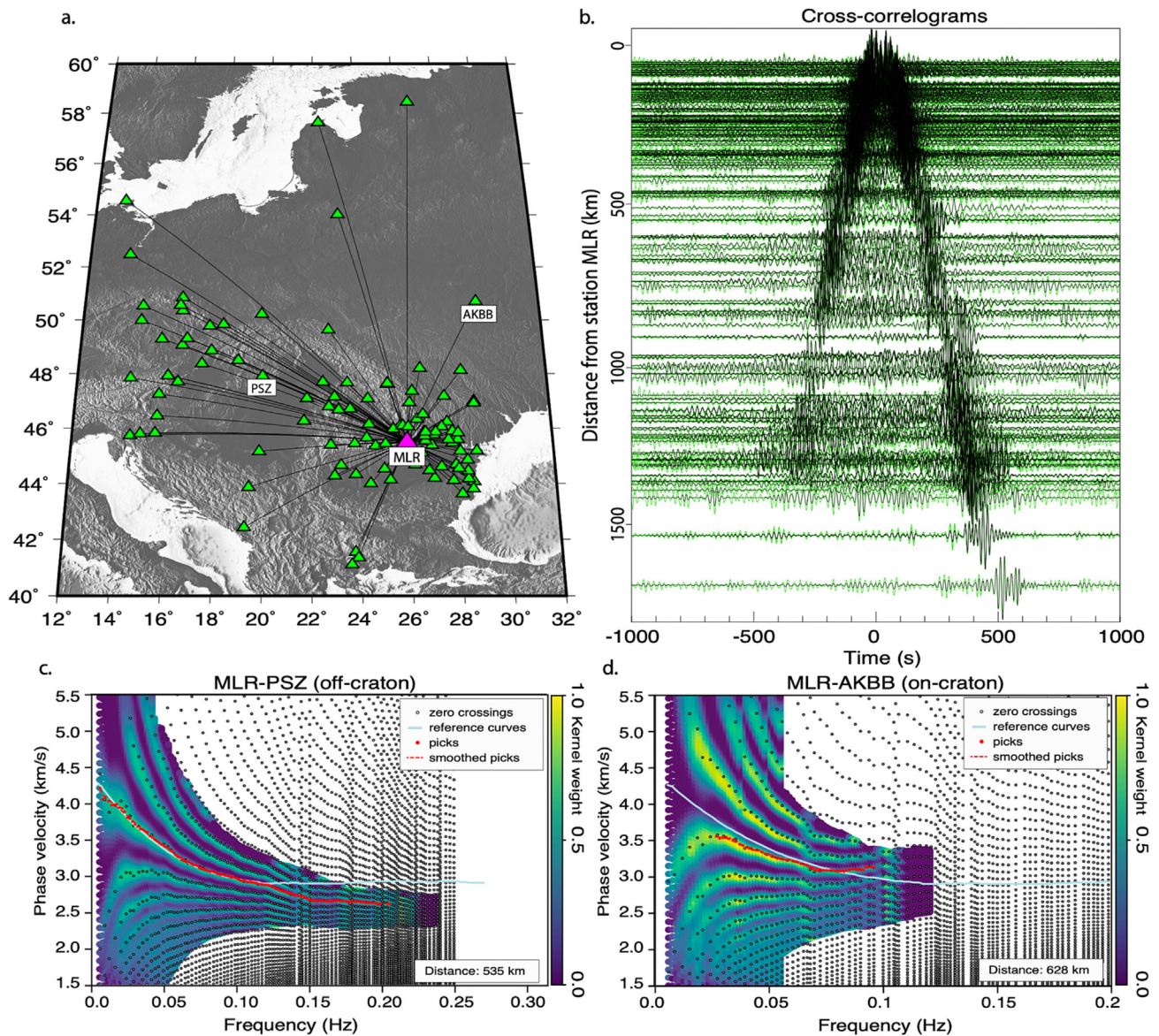
Fig. 2. a. Map showing a subset of seismic stations (green triangles), station mlr in romania (pink triangle) and inter-station virtual ray paths; b. record of cross-correlations between station mlr and selected stations plotted in a, showing clear surface wave packets in both causal and acausal cross-correlation branches. Green traces are the raw cross-correlograms and black traces are cross-correlograms denoised with the Continuous Wavelet Transform algorithm (Yang et al., 2020) which increases their signal-to-noise ratio; c, d. Examples of surface wave dispersion analysis between two pairs of stations. Colours indicate the heatmap produced from the summation of elliptical intensity kernels around zero-crossing picks (white circles). Dispersion values (red dots) are based on the resulting heatmap and do not coincide with zero-crossing picks. (For interpretation of the references to colour in this figure legend, the reader is referred to the web version of this article.)

gradient damping. We test a range of damping values under fixed smoothing and choose the value from the knee of the trade-off curve. The chosen values also depend on a visual analysis of resolution tests, aiming to suppress the leakage between mapped isotropic and anisotropic heterogeneities while not oversmoothing the maps (e.g. Darbyshire and Lebedev, 2009). The resulting values are similar for our period interval, ranging between 1 and 2 for lateral smoothing and 0.2 and 0.5 for gradient damping, respectively.

3.4. Probabilistic inversion

The phase velocity model is converted to the depth domain via a Markov chain Monte Carlo transdimensional Bayesian inversion (Bodin et al., 2012), which iteratively samples the model space and produces a final probability distribution on the model parameters (Fig. 3). We extract phase velocities from each grid knot at all periods and construct pseudo-dispersion curves at all coordinates

of our model. Each pseudo-dispersion curve is inverted individually using the probabilistic algorithm for a 1D shear wave velocity-depth profile. 1D profiles are then combined into a 3D shear wave velocity model.

We use the implementation of Dreiling and Tilmann (2019) where the search parameters include the shear-velocity in each layer, the average Vp/Vs ratio, the data noise level, expressed as the width, σ, of a Gaussian uncertainty distribution, and the number of layers. In the absence of a priori phase velocity measurement errors, the algorithm thus treats them as unknown hyperparameters to be determined in the Monte Carlo search. Errors (or alternatively referred to as noise) are assumed to be uncorrelated between data points at adjacent periods on the input dispersion function. The dimension of the model space (i.e. the number of layers) is itself a variable, making the posterior probability a transdimensional function. The model is allowed to vary between 2 km/s and 5 km/s without supplying a priori starting models,
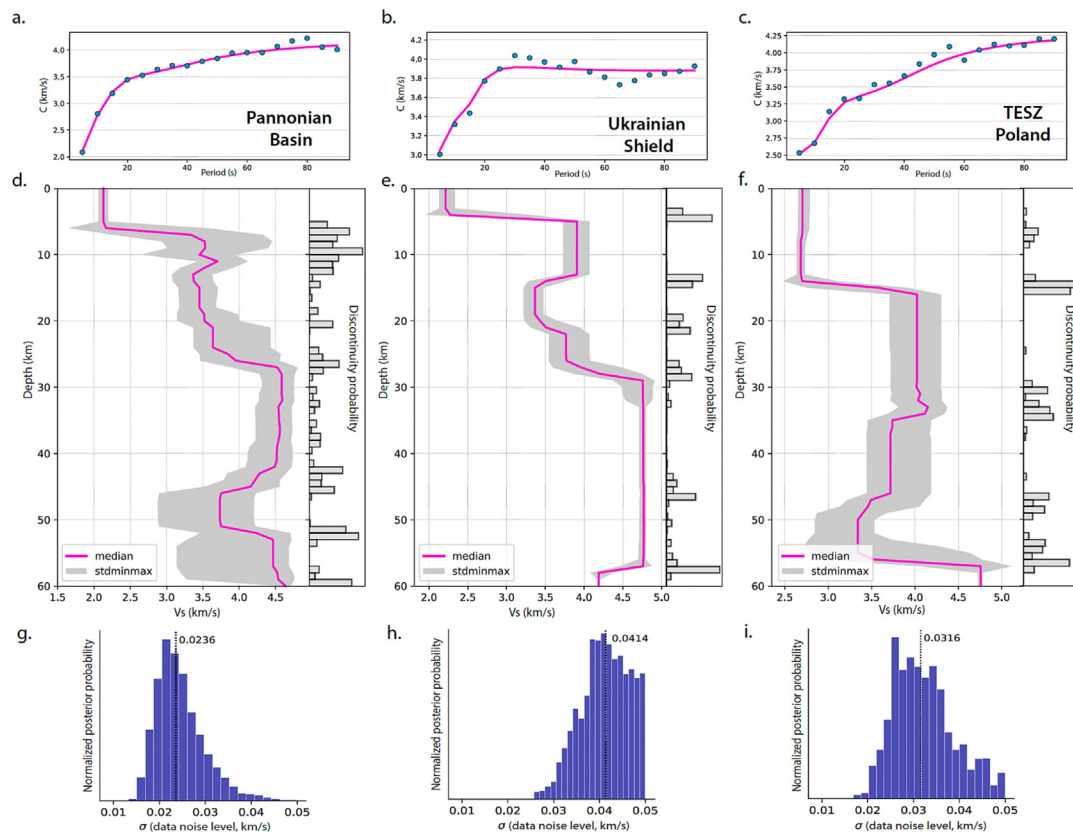
Fig. 3. Rayleigh wave phase velocity dispersion curves (a-c) and shear wave velocity (Vs) - depth profiles (d-f) for three selected regions in our study area. Dispersion curve data (black lines) are extracted from the phase velocity tomography and are converted to Vs-depth profiles with the McMc Bayesian inversion method. Pink lines are the best fit dispersion curve (a-c) and the median shear wave velocity profile (d-f) from the models ensemble. The shaded grey area is marked by the minimum and maximum standard deviation. Histograms represent the ensemble probability distribution that may be regarded as a discontinuity probability. The posterior probability distribution of data noise for each inversion (g-i). (For interpretation of the references to colour in this figure legend, the reader is referred to the web version of this article.)

measurement error bounds, or discontinuity depths. Other prior information consists of a user-set depth range between 0 and 60 km, a Vp/Vs interval of 1.5–2.0, a noise Gaussian width of 0–0.05 km/s and layer number of 3–20.

The inversion, or more accurately referred to as the forward model search, is carried out by running 5 separate model space samplers in parallel, each with a maximum of 50,000 iterations and a burn-in set of 10000. Each chain starts at different random points and samples the dynamic model space simultaneously and independently. The models explored in the burn-in set are discarded and those obtained in the exploration phase from each chain should achieve stability. The convergence of the algorithm is monitored via several metrics including acceptance rates, the evolution of the likelihood function or the misfit with iteration number (Figure S4 in the Supplementary Material). The outputs are combined in the end in an ensemble posterior probability that yields the best-fit velocity-depth profile. The expected value and associated uncertainty for each hyper-parameter (including Vs) are extracted as the mean and standard deviation of the posterior distribution (Figure S5 in the Supplementary Material).. The resolution of seismic discontinuities can be examined by projecting the ensemble of sampled Earth models into a marginal posterior distribution of Vs at each depth (Fig. 3). The existence of a seismic discontinuity is not a model parameter on its own so this function represents a probability density of having a discontinuity at each depth. The discontinuity probability is likely higher and sharper when the McMc sampler tends to produce more models with layer interfaces within a shorter depth interval.

Compared to a linear inversion with a high number of thin layers, the output models from the transdimensional inversion might yield profiles with sharp velocity-depth gradients especially when a lower number of layers is preferred. When the uncertainty is high, the algorithm tends to fit less complex models. Very thick layers as in Fig. 3e (30–55 km) are easily constrained and will thus show little variance because even a small change in Vs will have a relatively large impact on the data fit. A higher data noise region might result in a less complex model (with fewer layers) that might appear better constrained (lower standard deviation), because the sampler tends to fit only a few models. Such might be the case in the Ukrainian Shield inversion example (Fig. 3). On the other hand, a lower data noise region (e.g. the Pannonian Basin) results in a more complex model with an apparently higher uncertainty and lower discontinuity of probability at depths where changes in layer interface depths and velocity contrasts yield a similar data fit. We note, however, that surface waves are best at estimating absolute velocities, but lack the ability to resolve sharp vertical velocity changes, especially in the absence of an additional data type such as receiver functions. Additional bias may stem from inappropriate modeling assumptions such as the possibility of dipping layers or anisotropy. In the depth inversion, we only take the isotropic velocity components into account and do not model the azimuthal or radial anisotropy. These simplifications imply that we will not be able to perfectly fit the dispersion curves which may slightly increase the data uncertainty estimated during the model search.

4. Results

4.1. Resolution and leakage tests

Fig. 4 shows selected synthetic tests of phase velocity tomography demonstrating the ability of the inversion, model setup, and station configuration to recover various checkerboard anomaly patterns as well as possible rifting and deformation front anomalies. We define checkerboard patterns as low velocity anomalies (-2.5%) varying roughly between 200 km and 500 km in diameter embedded in a high velocity anomaly background (2.5%). We allow the inversion to produce anisotropy to also test for leakage between isotropic and anisotropic terms of Equation (1). In other words, we construct a purely isotropic model and check whether the inversion will create artefacts in azimuthal anisotropy.

The output synthetic models show variable recovery for different period maps, depending on ray coverage and azimuthal distribution. For the 40 s period, checkerboard patterns are well-recovered throughout Southern, Eastern, and Northern Europe,

and the Black Sea. Model resolution decreases at the edge of the Scandinavian Peninsula, across the Baltic Sea, in northeast Belarus and Eastern Ukraine. Here, the shape of the smaller checkerboard patterns are still recovered, but anomalies show half the original amplitudes (Fig. 4). The larger checkerboards show a better anomaly recovery in Eastern Ukraine compared to smaller checkerboards. For the 10 s period map, the amplitude of small-scale anomalies decrease to half of the original value in Ukraine, Poland and fade completely to the north-east. At lower periods, the Black Sea synthetic anomalies are smeared towards the east along the dominantly E-W trending ray paths (<15 s). Artifact anisotropy produced in the inversion is negligible at all periods.

We also test the resolution of possible low velocity anomaly features simulating the general trends of the TESZ, the Central Russian Rift System, and the Dnieper-Donets Rift (Fig. 1). Fig. 4 shows near-perfect recovery of the synthetic TESZ anomaly at both short and long periods, as well as the intersecting region with the Central Russian Rift System, while its northeastern section and the Dnieper-Donets Rift shapes are preserved, albeit with reduced
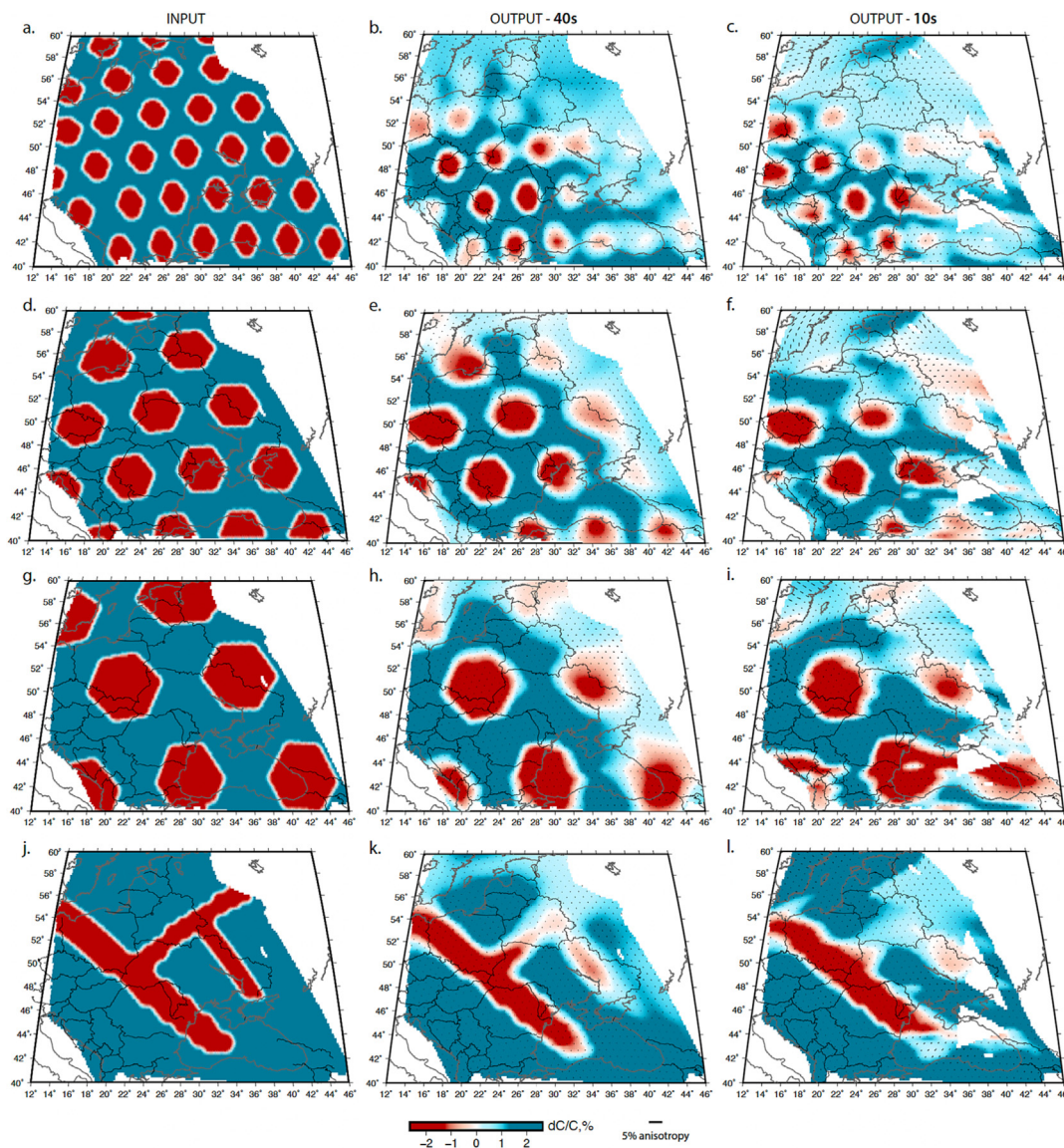

Fig. 4. Resolution tests for isotropic phase velocity tomography. The left column (a,d,g,j) comprises a range of input synthetic models (checkerboard patterns with 2.5% phase velocity peak anomalies and paleorift simulations). The middle (b,e,h,k) and right columns (c,f,i,l) show recovered models for the 40 s and 10 s period maps, respectively.

amplitude at longer periods. Anisotropy artefacts are insignificant throughout the model region for this specific anomaly pattern.

4.2. Phase velocities - isotropic variations and azimuthal anisotropy

Models of phase velocity anomalies and azimuthal anisotropy are shown in Fig. 5. Since the grid area varies with period, isotropic phase velocities are only determined at grid knots along inter-station ray paths. However, model resolution decreases especially in areas with low ray density and/or uneven azimuthal distribution (see insets in Fig. 5 for each period). We mask phase velocity and anisotropy regions with low model credibility using these criteria, in conjunction with checkerboard recovery tests at each period.

Phase velocities show excellent correlation between negative anomalies and known sedimentary basins at short periods (5–10 s) sensitive to uppermost crustal depths (depths ~5-15 km, Fig. 5), demonstrating the power of ambient noise to resolve near-surface structures. Low velocities follow the arcuate Carpathian foreland basins, the South Carpathian foredeep and the Paleozoic cover of the Moesian Platform, the Pannonian Basin, the Transylvanian Basin, the Western Black Sea Basin, as well as

the *peri*-Tornquist Basins. The surface expression of the TESZ roughly corresponds to an elongated low-velocity zone at periods of 5 s and 10 s, with parallel NW-SE oriented azimuthal anisotropy in the Polish sector and oblique-to-perpendicular across the Carpathians (Fig. 5). The negative velocity patch seems to join the Eastern Carpathians foredeep low velocity signature arching around the orogen. At longer periods (15–25 s; depths ~15-30 km), the TESZ seems to separate low velocities on its western side and higher velocities to the eastern side, especially across the Carpathian sector.

At periods of 20 s-30 s (depths ~15-35 km), another NW-SE oriented elongated low velocity anomaly, quasi-parallel to the TESZ, emerges within the East European Craton. This anomaly as well as anisotropy directions appear to wrap around high velocity centers that correspond to exposed Archean and Paleoproterozoic basement of Sarmatia (yellow contours in Fig. 5).

At longer periods (40 s-50 s; depths ~35-60 km), indicative of lower crust- uppermost mantle depths, maps are dominated by increased heterogeneity. Consistently low velocities follow the surface expression of the Dnieper-Donets Rift (Fig. 1) and anisotropy seems mostly oblique to the general rift axis.
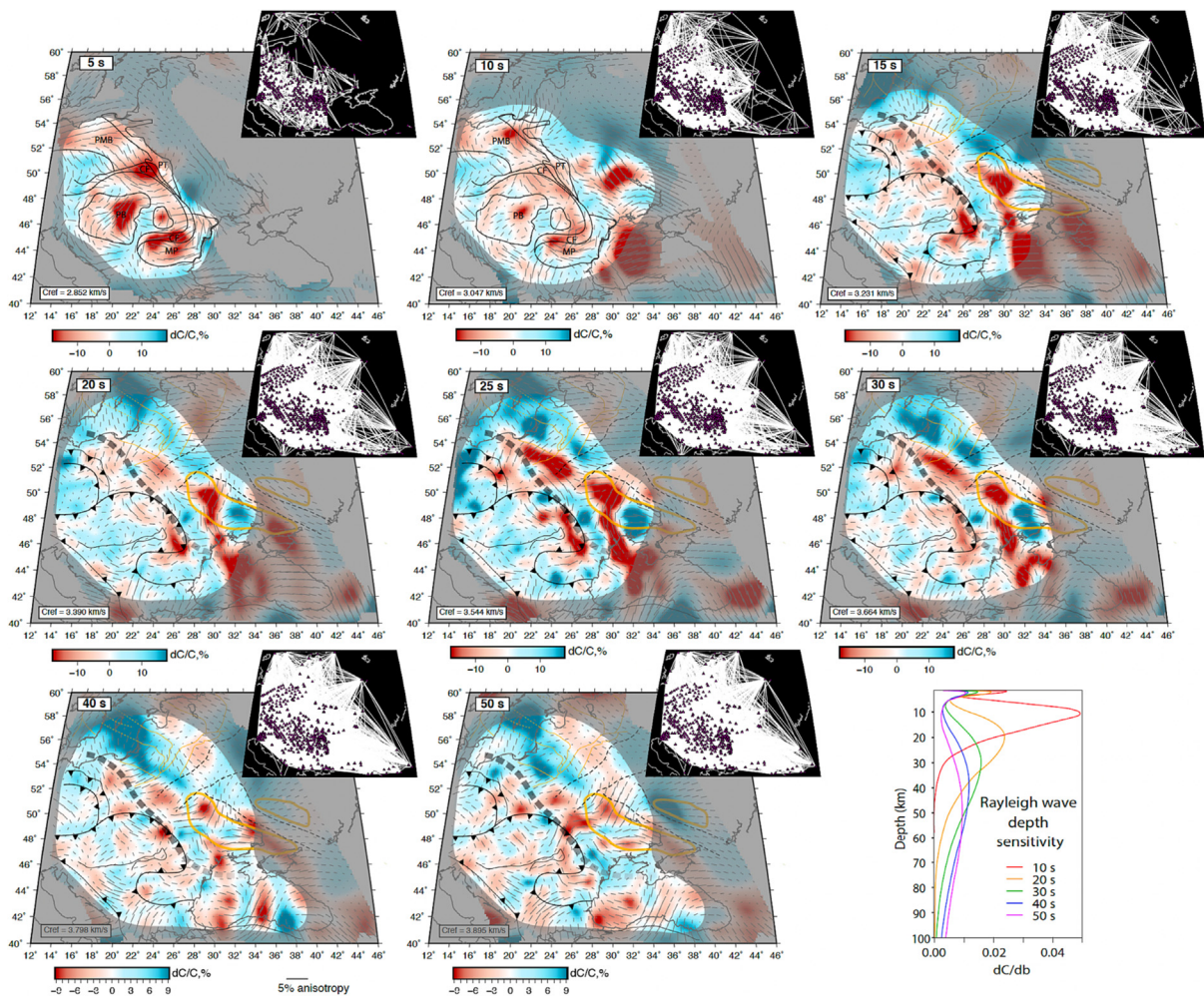

Fig. 5. Phase velocity maps of Central, Eastern and Northern Europe at periods between 5 s and 50 s. The colour scale indicates isotropic phase velocities and changes with period, and lines mark the amplitude and direction of azimuthal anisotropy. The 5 s and 10 s maps are overlain with the approximate boundaries of the main sedimentary basins in Europe after Fig. 1d. Abbreviations are. PMB - Paleozoic-Mezosoic Basins, CF - Carpathian Forearc, MP - Moesian Paleozoic Basin, PB - Pannonian Basin, TB - Transylvanian Basin, PT - Peri- Tornquist Basins, WBS - West Black Sea Basin. Longer period maps are overlain with the main geological boundaries and tectonic regions as in Fig. 1a. Insets show the virtual ray coverage at each period. Bottom right. Rayleigh wave depth-sensitivity kernels to isotropic shear wave speed for selected periods (shown for reference, not used in the inversion).
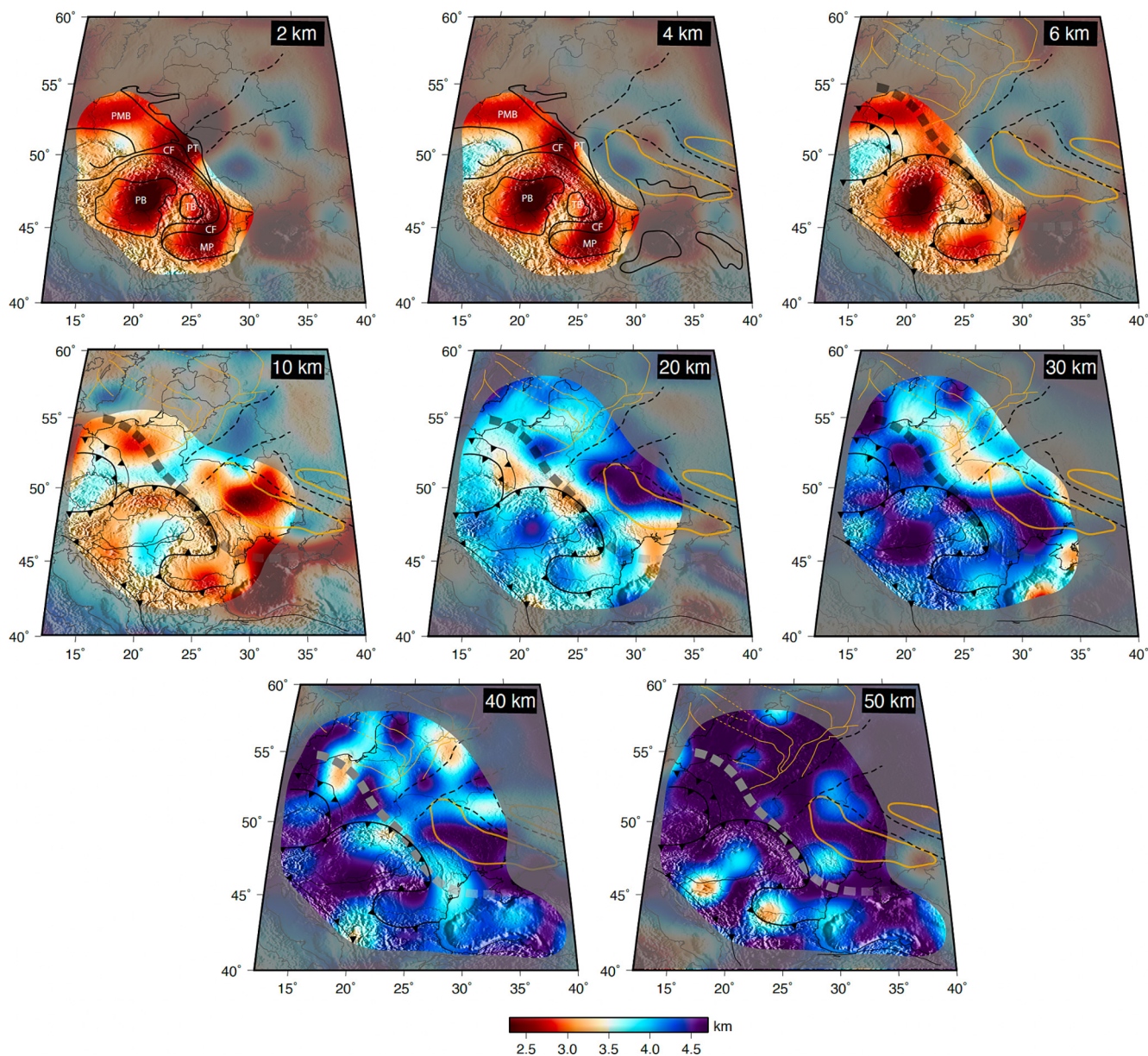
Fig. 6. Shear wave velocity maps of Central, Eastern, and Northern Europe at selected depth slices from our transdimensional velocity model, overlain with major geological boundaries as in Fig. 1a and political boundaries.

4.3. Shear wave velocity tomography

Fig. 6 shows the shear wave velocity model estimated with the probabilistic transdimensional inversion algorithm. Here, we mask shear wave velocity regions similarly to the phase velocity maps, according to the peak depth sensitivity of Rayleigh waves at each period (Fig. 5). The relationships between periods and depths are not straightforward. Depth sensitivity functions for Rayleigh waves of various periods have different degrees of overlap in the upper crust. Thus, the masking choice for the shear wave velocity model is not entirely dictated by the availability of phase velocity measurements at specific grid points. The shear wave velocity model shows heterogeneous patterns across Central and Eastern Europe (Fig. 6). Model uncertainties consist in standard deviations estimated based on posterior probability functions for Vs at each depth slice (Figure S5 in the Supplementary Material). These vary between 0 and 0.8 km/s, with an average of 0.18 km/s at 5 km depth, 0.27 km/s at 20 km depth and 0.25 km/s at 40 km depth.

These errors are significantly lower than the estimated seismic heterogeneities, allowing us to confidently constrain differences between felsic and mafic rocks, for example, for which seismic velocity changes were estimated as high as 2 km/s (e.g. Rudnick and Fountain, 1995). In the absence of measurement errors, the transdimensional code also searched for the level of noise in the velocities extracted from the phase-velocity maps, yielding an average σ value of 0.035 km/s (Figure S6 in the Supplementary Material).

At shallow depths (<6 km), low velocity values correlate with the location of known sedimentary basins (Fig. 6). The Pannonian Basin is the most prominent anomaly, emerging as a low velocity feature that persists down to ~6 km. The Carpathian foreland basin, especially the southern section, have similarly low velocity signatures down to ~10 km, likely sampling Neogene and Paleozoic sedimentary successions from different past orogenies. The *peri*-Tornquist Basins and the TESZ correspond to low velocity regions that fade out at depths > 6 km, compared to the

off-craton basins. The Osnitsk-Mikashevich Igneous Belt is overlain by a seismically slow layer down to at least ~2 km, corresponding to the Late Palaeozoic Pripyat Trough (Fig. 1a, c and 6).

High velocities across part of the Ukrainian Shield and the Osnitsk-Mikashevich Igneous Belt (Fig. 6), roughly correspond to the lateral extent of the Volyn igneous province (Fig. 1) and the exposed basement regions of Sarmatia. The Ukrainian Shield displays a high velocity feature at upper and lower crustal depths separated by a thin low velocity layer at ~10 km depth.

At lower crustal depths, the shear wave velocity becomes increasingly complex and apparently independent of the surface geology. Cross-sections show several seismic velocity changes and discontinuity offsets across the deformational fronts and the TESZ (Fig. 7), but also significant crustal seismic velocity heterogeneities

within the East European Craton terranes. The Fennoscandian orogens seem underlain by a mostly uniform crust with a flat Moho, while Sarmatia shows strong lateral heterogeneities. A regional scale low-angle dipping interface underlies the Ukrainian Shield, the Scythian Platform and the Crimea Peninsula.

5. Discussion

5.1. Comparison with previous seismic tomography models

Most continental and global seismic tomography models of the mantle based on earthquake data show a strong contrast between the high seismic velocities to the east of the Trans-European Suture
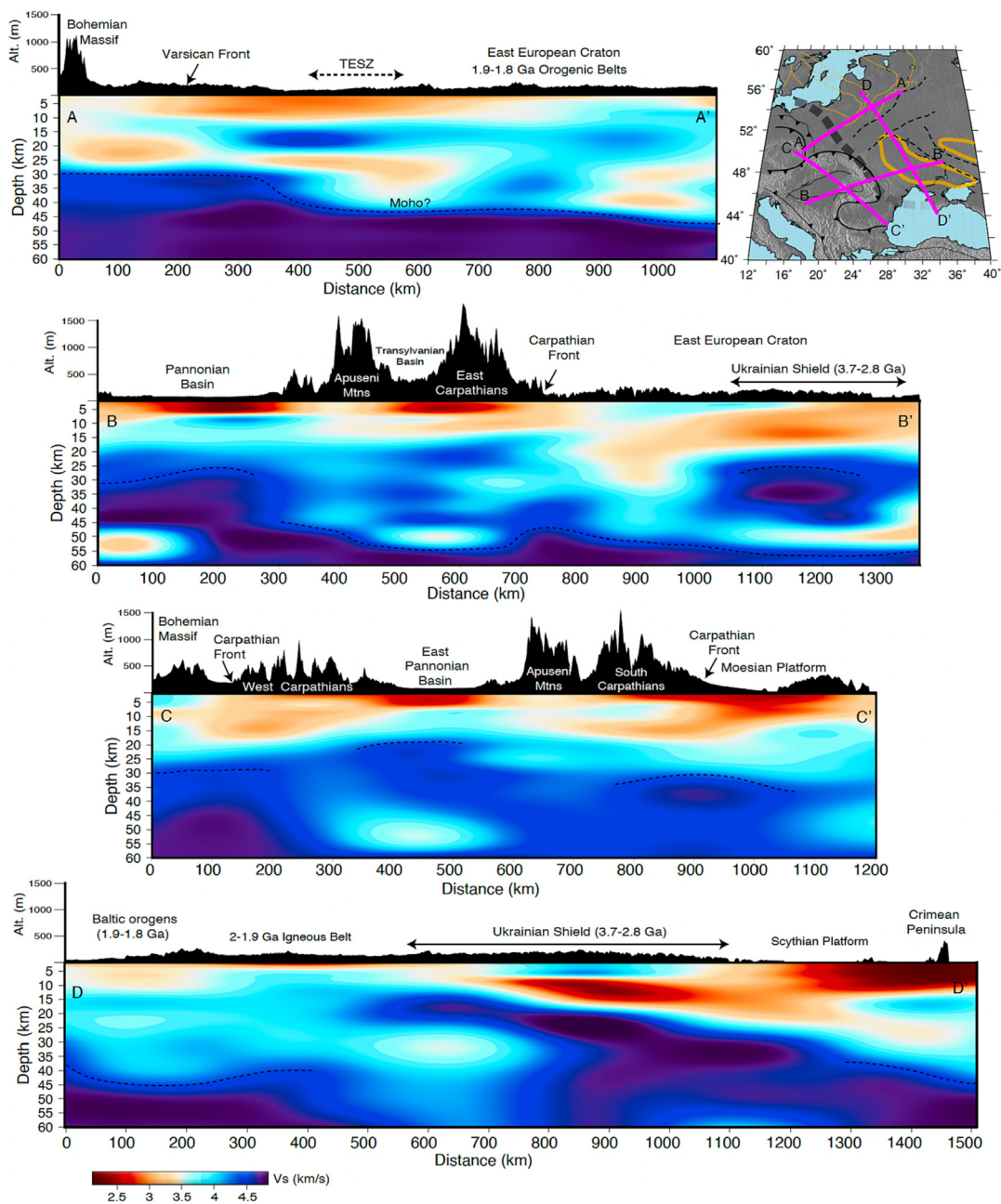

Fig. 7. Cross-sections of shear wave velocity through the crust and uppermost mantle across and parallel to the Trans European Suture Zone. An exaggerated topography is shown above each profile. Dashed black lines are interpreted traces of the Moho discontinuity. Top right. Topographic map of Europe showing the major geological boundaries and pink lines corresponding to the cross-sections. (For interpretation of the references to colour in this figure legend, the reader is referred to the web version of this article.)

Zone and seismically slow regions south-west of the TESZ at ~100 km depth (e.g. Yang et al., 2007; Chang et al., 2010; Schivardi and Morelli, 2011; Legendre et al., 2012; Schaeffer and Lebedev, 2013; Zhu et al., 2015). In contrast to our study, these models lack the dense seismic station and ray coverage in the Eastern European Platform we benefit from and often, likely due to model edge resolution decrease, they portray the EEC mantle as a wide, seismically fast, homogenous lithospheric root, despite its protruded and complex tectonic history that includes multiple collisions, rifting, and volcanism.

Seismic heterogeneities in the shallow lithosphere above 100 km show more complex heterogeneities than a constant SW-NE gradient across the TESZ, but bear many similarities with local and partially overlapping ambient noise tomography models that are sensitive to crustal levels. These include, but are not limited to, the models of Ren et al. (2013), Meier et al. (2016), Soomro et al. (2016), Lu et al. (2018), and Szanyi et al. (2021). The models of Ren et al. (2013), Lu et al. (2018) and Szanyi et al. (2021) partially overlap with our study area in the the Carpathian-Pannonian Region (Ren et al., 2013) and the Pannonian-Eastern Alpine region (Lu et al., 2018; Szanyi et al., 2021). All models show slow seismic anomalies in the Pannonian, Transylvanian, and Carpathian Foreland basins, similar to our model at low periods/shallow depths. High velocities emerge at 10–20 km depth beneath the Pannonian compared to the surrounding orogenic structures, consistent with our model, and interpreted as a thinned crust beneath the basin (Ren et al., 2013; Szanyi et al., 2021). The ambient noise phase velocity model of Soomro et al. (2016) covers central Europe, overlapping with our study area north of 45° N and west of 25° E. We note several similarities between our phase velocity maps and the Soomro et al. (2016) heterogeneities, specifically the contrast between the high seismic velocity Bohemian Massif and the low-velocity Permian Basins extending across Poland and Germany at periods up to 20 s (Fig. 5). At longer periods (>40 s, both in our model and in the model of Soomro et al. (2016), the TESZ section across Poland seems to mark a transition from low-to-high seismic anomalies (Fig. 5). Our model shows, however, that this transition is only consistent in the Baltic region. Further south-east along its probable trajectory, the TESZ marks a switch from high-to-low velocity anomalies near the Orsha-Volyn Aulacogen and low-to-high along the Carpathian Front in Romania (40 s and 50 s maps, Fig. 5).

5.2. Azimuthal anisotropy - past or present deformation?

While shear wave velocity heterogeneities can offer fundamental clues on compositional variations, temperature, or water content, anisotropy provides complementary information that can shed light on a range of active or past deformation mechanisms affecting lithospheric structure (e.g. Long and Becker, 2010). There are two primary candidates for observed seismic anisotropy. Intrinsically anisotropic minerals such as olivine in the mantle or biotite and hornblende in the crust (e.g. Mainprice and Nicolas, 1989) develop lattice-preferred orientation (LPO) along the maximum shear direction (Nicolas and Christensen, 1987) or the maximum extension direction (e.g. Ribe, 1992) and are often interpreted as evidence of mantle flow (e.g. Karato et al., 2008). Shape-preferred orientation (SPO) of fault zones (Boness and Zoback, 2006), cracks, or inclusions (Crampin, 1994) such as magmatic intrusions (Kendall et al., 2005) or rift axes (e.g. Bastow et al., 2010) can also cause seismic anisotropy. Discriminating between these opposing mechanisms can be difficult, especially because the direction of anisotropy can vary relative to maximum extension. For example, SPO anisotropy from alignment of cracks in the crust is perpendicular to the maximum extension, but LPO anisotropy in the mantle is parallel to maximum extension (Fouch and

Rondenay, 2006). Thus even in a simple crust-mantle coupling model, a complex signal can be observed.

Lithospheric anisotropy in Central and Eastern Europe has often been interpreted as frozen deformation inherited from past tectonic events in the EEC (Wüstefeld et al., 2010) and the accretion of younger microplates (e.g. Babuška and Plomerová, 2006). Recent anisotropic seismic tomography models of European lithosphere (Zhu et al., 2015; Nita et al., 2016) support an anisotropic block-model of Europe as suggested by Plomerová et al. (2011). Zhu and Tromp (2013) notes that anisotropy in the EEC tends to align along ancient rift systems, such as the Central Russia Rift System and the Pripyat-Dnieper-Donets Rift and dipping anisotropy is likely present beneath the Ukrainian Shield. We note, however, that these models offer anisotropic constraints mostly from the lower crust and the underlying mantle, while our ambient-noise frequency range allows the extraction of seismic information from the entire crustal column.

Azimuthal anisotropy at short periods (sensitive to shallow depths) is strongest (~5%) in the low-velocity sedimentary basins (Fig. 5). At depths < 5 km, bulk anisotropy may be dominated by microcracks, according to laboratory experiments (Kern, 1990). Fluid-saturated microcracks are highly sensitive to small changes of stress (Crampin and Peacock, 2008). The Pannonian Basin is undergoing tectonic inversion due to the continuous push of Adria approximately towards the NE. A NE-SW oriented fault boundary between Alcapa and Tisza underlies sedimentary sequences (Fig. 1a), likely contributing to the observed anisotropy trends, as would be expected from fault-aligned anisotropy (Boness and Zoback, 2006). In the South Carpathian Foreland basin and the Moesian Platform Basin (Fig. 1a), anisotropy is also strong and oriented E-W, along the obliquely juxtaposed Carpathian nappes (Fig. 5). The region is tectonically active as suggested by the many shallow-depth seismic swarms that occurred along the front (e.g. Radulian et al., 2019; Borleanu et al., 2023). In the PMB, anisotropy rotates clockwise from SE-NW near the Baltic Sea to NE-SW near the Carpathian Front and TESZ. Here, anisotropy is less likely controlled by an active stress field. The correlation with the surface-expression of the TESZ and Variscan Front rather points to a frozen deformation pattern caused by the past collisional events associated with these tectonic boundaries.

The EEC crust exhibits complex patterns of anisotropy with variable strength that are most likely inherited from past tectonic events. The Baltic orogens of Fennoscandia exhibit mostly SE-NW oriented 2–3% anisotropy at all depths, oblique to the tectonic boundary trends. Anisotropy clearly switches to NE-SW across the Central Belarus Suture Zone and the Osnitsk- Mikashevich Igneous Belt, part of the Central Russian Rift System. Here, anisotropy strongly decreases at longer periods (40–50 s, Fig. 5, sensitive to lower crust/upper mantle levels). This observation is in contrast to the rift-aligned axes estimated by Zhu and Tromp (2013) at depths > 50 km, implying a different mechanism at depth. The Ukrainian Shield is strongly anisotropic (3–5%) and seems divided in two main domains with contrasting fabrics and seismic velocities.

5.3. The TESZ and stacked collisional fronts: Imaging lateral continental growth

Our new lithospheric tomography captures a number of significant geological boundaries such as the TESZ, associated with the Caledonian Front, as well as the Variscan, and the Carpathian Fronts, marking the lateral growth of the European continent and, more fundamentally, a transition zone separating Phanerozoic from Precambrian tectonic processes. We attempt to explain the most prominent features in our tomography in relation to those boundaries and the lithospheric fragments they demarcate,

although correlations with surface geology are not always straight-forward at depth.

At uppermost crustal levels, the TESZ does not seem to clearly separate regions of high and low velocity (Fig. 6), as was often imaged at asthenospheric depths (e.g. Bijwaard and Spakman, 2000; Zhu et al., 2012). Its route, width, and complexity change along-strike from Poland where it appears as a broad low velocity zone suggesting the presence of a thick sedimentary basin (e.g. Grad et al., 2003) while its southeastern segment is buried beneath the Carpathian Orogen (Starostenko et al., 2020; Borleanu et al., 2021). Anisotropy patterns (Fig. 5) also show many period-dependent changes across and along the TESZ, indicating complex layered deformation across the craton edge. Profile AA' in Fig. 7 shows an increase in upper mantle velocities towards the north-east, from Avalonian terranes towards the EEC, consistent with decreased density of cratonic lithosphere (Artemieva, 2003). The TESZ is marked at depth by a lateral change in lower crustal velocities and a ~20 km depression of what might be considered the Moho discontinuity based on the sudden Vs increase to typical mantle wave speeds (Fig. 7). These crustal thickness and seismic velocity changes may be the consequences of Avalonia- Baltica collision and possible slab break-off and are corroborated by previous receiver function studies (Knapmeyer-Endrun et al., 2014), local ambient noise studies (Becker and Knapmeyer-Endrun, 2018) and all the active seismic surveys crossing this boundary north of the Carpathian Front: EUROBRIDGE97 (Yliniemi et al., 2001), POLO-NAISE97 (Guterch et al., 1999; Grad et al., 2002), as well as those that cross the Carpathians towards the Osnitsk-Mikashevich Igneous Belt: the CELEBRATION00 (Grad et al., 2006) and PANCAKE (Starostenko et al., 2013) profiles (Fig. 1d).

Grad et al. (2003) suggested several scenarios for the type of collision that reworked the passive EEC margin, including flake tectonics (e.g. Meissner, 1989) or a soft or oblique collision. In the flake tectonic model, Baltica presumably indented into Avalonia, obducting its upper crust and forcing its lower crustal layer beneath the indenter. Profile AA' (Fig. 7) shows a high velocity mid-crustal layer (~4 km/s) sandwiched between comparatively lower velocity layers (also evident in probability of discontinuity cross sections in Figure S8). This layer extends beyond the TESZ and the surface expression of the Variscan Front and pinches out beneath the Bohemian Massif. The high velocity layer seems connected to the broader high velocity EEC crust belonging to the Fennoscandian Paleoproterozoic orogens, supporting the idea that Precambrian crust might form an extensive wedge embedded into more juvenile terranes accreted during Phaneorozoic orogeneses. From an anisotropic point of view, the TESZ in this region marks a reorientation of oblique to perpendicular fast axes at periods < 40 s and a more clear switch from TESZ-parallel to TESZ-perpendicular at 40–50 s (lower crust). This gradual change in anisotropy at mid-lower crustal levels underlain by a more rapid rotation at lower crustal levels might support the indenter tectonic style. Similar mechanisms have been proposed for the Slave craton in Canada based on the LITHOPROBE seismic surveys (Snyder, 2002).

The seismic structure of the TESZ changes dramatically along its southwestern segment, across the Eastern Carpathians. Here, the TESZ may be underthrusted and overprinted by Neogene orogeny and post-collisional volcanism (Borleanu et al., 2021) and anisotropy seems largely oblique to perpendicular to the orogenic trend at least in the Eastern Carpathians suggesting horizontal tectonics in the thickened crustal root similar to the lower crustal fabrics of the Central Alps (Fry et al., 2010). Profile BB' in Fig. 7 shows a strong change in crustal velocity patterns and a depression of the 4.5 km/s contour beneath the Carpathians. Beneath the Ukrainian Shield region, Vs reaches mantle-typical values at depths of ~30 km overlying a low velocity zone at ~50 km. Discontinuity

probability profiles in this area also show two strong peaks between 15 and 20 km depth and one peak between 50 and 55 km depth (Figure S8). This profile is close to the RomUkrSeis seismic profile (Fig. 1d, Starostenko et al., 2020) which shows similar crustal fabrics, including a local crustal thickening beneath the Carpathians and thinning towards the northeast.

5.4. Crustal and lithospheric thinning beneath the Carpathian-Pannonian region

The Carpathian Orogen shows variable seismic structure along-strike and significant crustal and lithospheric thinning in the enclosed Pannonian Basin. Compression in the Carpathians along the EEC margin is generally thought to be coeval with backarc extension in the Pannonian, possibly driven by a retreating subduction zone towards the craton (e.g. Royden, 1988) or lateral extrusion of the Eastern Alps (e.g. Ratschbacher et al., 1991). The Pannonian Basin is superimposed on several microplates that sutured before the Carpathian Orogen. The Tisza- Dacia collision led to the closure of a Neo-Tethys branch (Schmid et al., 2008) whose ophiolitic remnants are partly exposed in the Apuseni Mountains and mostly buried beneath the Pannonian and Transylvanian basins (Fig. 1). Our model shows a stark contrast in crust and mantle velocity patterns across the Apuseni Mountains (Profile BB' in Fig. 7), which, along with the Transylvanian Basin region, acted as a transfer zone between contracting and extending regions (Huismans and Bertotti, 2002). Similarly to previous studies (Ren et al., 2013; Petrescu et al., 2019), our model shows low seismic velocities down to depths of ~50 km beneath the Apuseni Mountains and Transylvania, with variably clear Vs discontinuities (Figure S8). In contrast, the seismic profile of the Pannonian Basin (Fig. 3) shows a thin crust (Vs values reach typical upper mantle velocity at ~25 km) and an anomalously shallow lithosphere-asthenosphere boundary marked by a decrease in Vs at 45–50 km depth. Discontinuity profiles show a large probability at ~6 km and two secondary peaks between 15 and 25 km (Figure S8). These observations are consistent with both passive seismic data studies (e.g. Kalmár et al., 2021) and active seismic surveys (Posgay et al., 1981) and support the existence of a hyper-extended lithosphere and shallow asthenosphere.

The Carpathian Front captured in Profile CC' is marked by an uplift of the 4 km/s Vs contour, a decrease in upper mantle velocities and a zone with less discernible crust-mantle Vs discontinuities beneath the Western Carpathians, corroborating the SUDETES2003 seismic profile (S04 in Fig. 1d, Hrubcová et al., 2010). This change is not replicated on the opposite section of the Carpathian Front, marking the collision between the Tisza-Dacia unit and the Precambrian block of Moesia (Fig. 1). This section shows gradual crustal thickening beneath Moesia and what is likely the dipping low velocity Paleozoic sedimentary cover of Moesia beneath the South Carpathians (Profile CC' in Fig. 7). Seismic structures of the East and South Carpathians are markedly different, likely due to the type of lithosphere involved in the collision. While the East Carpathians are a classic fold-and-thrust belt overlying an already complex zone of reworked craton margin, the South Carpathians were obducted obliquely onto the Moesian Platform (e.g. Hippolyte et al., 1999), with reduced impact on its crustal structure and strong lithosphere.

5.5. Seismic expression of tectonic units in the East European Craton

The oldest and most enigmatic continental fragments captured with our tomography date back to the Archean, when the Earth might have been too hot to sustain modern plate tectonics (e.g. Korenaga, 2013). The East European Craton has been involved in multiple collisions, and subject to episodes of extension and

magmatism before it reached the present-day tectonic stability (e.g. Mints, 2015). The most prominent uppermost crustal feature is the high velocity anomaly roughly corresponding to the exposed crystalline basement of the Ukrainian Shield (Fig. 1). This anomaly strongly contrasts with the nearby low velocity region of the 2–1.95 Ga Osnitsk-Mikashevich Igneous Belt, covered with up to ~4 km of sediments, and the Baltic orogens of Fennoscandia (Fig. 6). The anomaly expands at ~4 km depth, consistent with the location of the large 1.8–1.7 Ga Korosten pluton (Thybo et al., 2003). This high velocity anomaly is underlain by a mid-crustal low velocity zone overlying a high velocity layer (Fig. 3e). The alternation of high and low velocity layers in this region mirrors a depth and period-dependent change in azimuthal anisotropy (Fig. 5) and is similar to the EUROPROBE'97 seismic profile (EB97 in Fig. 1d, Thybo et al., 2003), indicating a highly complex crustal structure in contrast with the relatively uniform crust of Fennoscandia to the north (Fig. 7). The low velocity layer at ~10 km beneath the US (Fig. 7) corresponds with a low velocity layer at similar depth in the EB97 (Thybo et al., 2003) and gravity modeling indicates the presence of interlayered anorthosites and granitoids with Vp as low as 6 km/s and density as low as 2.6×10^3 kg/m^3 (Yegorova et al., 2004).

Probably the most intriguing feature of our model of the EEC is the large-scale low-angle south-dipping interface that extends beneath the Ukrainian Shield, the Scythian Platform, and beneath the Crimean Peninsula (Profile DD', Fig. 7). The DOBRE-4 seismic survey intersects our profile DD' in the south (Fig. 1d) and confirms the existence of a high-impedance discontinuity at ~25 km depth (Starostenko et al., 2017). A deeper velocity interface emerges in profile BB' at ~50 km depth, consistent with the location of sub-crustal reflectors identified on the RomUkrSeis seismic profile beneath the Shield (Starostenko et al., 2020). In discontinuity probability profiles, the interface appears like a rough step-wise lateral deepening of a layer interface (profile DD' in Figure S8). The presence of this low-angle dipping interface has also been suggested by Zhu et al. (2015) as dipping anisotropy and places fundamental constraints on the geodynamic regime dominant at the time of crustal formation. Specifically, it supports a crustal growth mechanism driven by lateral rather than vertical tectonics (e.g. Jain et al., 2019), which would have included diapiric doming of magmatic structures with a chaotic internal geometry (Van Kranendonk et al., 2004). Whether the thermal and rheological state of the Precambrian or earlier mantle allowed subduction processes or the Earth was dominated by mantle-plume dynamics and convection overturns remains a matter of debate (Gerya, 2014). Similar features appeared in the Archean terranes of the Superior craton in Canada and were interpreted as relict 2.7 Ga subduction-associated sutures (Calvert et al., 1995), supporting an accretionary scenario for continental growth at least at that particular time and location. However, the Scythian Platform, often regarded as the passive margin of the EEC, was affected by Early Paleozoic orogeny (Saintot et al., 2006), and the Crimean Peninsula experienced Cenozoic shortening due to the collision of the southern margin of Eurasia with several continental microplates (Hippolyte et al., 2018). Thus, younger compressional pulses might have overprinted older Archean fabrics, shedding doubt over the age of this regional scale interface.

6. Summary and conclusions

We investigated the crustal and uppermost mantle structure of Central, Eastern and Northern Europe, using the most recent tools for processing seismic ambient noise recorded at all.

available broadband seismic stations that operated in the region between 1999 and 2020. A new shear wave velocity model is constructed based on Rayleigh wave phase velocity dispersion curves obtained from empirical Green's functions estimated between pairs of seismic stations that operated simultaneously. We build our model in two steps. We first use an LSQR inversion method to estimate isotropic and anisotropic phase velocity anomalies on a regular grid. Secondly, we use a *trans*-dimensional Markov-chain Monte Carlo method to invert the frequency-domain tomography to a depth-domain shear wave velocity model.

We discuss the seismic signature of the stacked orogenic fronts that successively reworked the margin of the EEC and confirm the existence of multiple offsets of shear wave velocity discontinuities in the lower crust beneath the TESZ and a general increase in seismic velocity in the mantle. These observations point to a thicker crust and a more depleted craton lithosphere on the eastern side of the TESZ. High velocity crustal wedges extend beyond the TESZ in the Polish section, supporting a flake tectonic style in this area, in which cratonic crust indents into younger European terranes accreted during collision with Avalonia.

In the Carpathian-Pannonian region, our model is consistent with a hyper-extended crust and thin lithosphere beneath the Pannonian Basin, in contrast to a thick low velocity lithosphere beneath Apuseni Mountains and the Transylvanian Basin, the locus of Mesozoic assembly of a series of continental fragments and ophiolite obduction. The stark difference between the lithospheres of the Pannonian and Transylvanian Basins may be relevant for testing the hypothesis of slab-roll back, generally thought to have driven extension throughout the region. The model also shows significant heterogeneities along the Carpathians, reflecting a changing collisional style along their sinuous track.

The major Precambrian units of the EEC exhibit contrasting seismic structure: while Fennoscandia is underlain by a relatively homogeneous crust with flat seismic discontinuities, Sarmatia comprises alternating high and low velocity layers, likely representing mafic plutons emplaced during multiple Proterozoic magmatic episodes. A large-scale south-dipping interface appears to extend beneath the Ukrainian Shield and the Crimean Peninsula, favoring a geodynamic regime dominated by horizontal tectonics in this area. The dipping discontinuity may be a preserved Precambrian suture zone or a deformational overprint due to younger orogeneses at the southern rim of Baltica.

CRediT authorship contribution statement

Laura Petrescu: Conceptualization, Formal analysis, Visualization, Writing – original draft, Investigation, Funding acquisition, Project administration. **Felix Borleanu:** Data curation, Formal analysis, Writing – review & editing. **Emanuel Kästle:** Software, Writing – review & editing. **Randell Stephenson:** Writing – review & editing. **Anica Plăcintă:** Data curation. **Oleksandr Ivanovich Liashchuk:** Data curation.

Declaration of Competing Interest

The authors declare that they have no known competing financial interests or personal relationships that could have appeared to influence the work reported in this paper.

Acknowledgments

Appendix A. Supplementary data

Supplementary data to this article can be found online at https://doi.org/10.1016/j.gr.2023.08.022.

References

Artemieva, I., 2003. Lithospheric structure, composition, and thermal regime of the East European Craton: Implications for the subsidence of the Russian platform. Earth Planet Sci. Lett. 213, 431–446. https://doi.org/10.1016/S0012-821X(03)00327-3.

BABEL Working Group, 1993. Deep seismic reflection/refraction interpretation of crustal structure along BABEL profiles A and B in the southern Baltic Sea. Geophys. J. Int. 112 (3), 325–343.

Babuška, V., Plomerová, J., 2006. European mantle lithosphere assembled from rigid microplates with inherited seismic anisotropy. Phys. Earth Planet. Int. 158 (2–4), 264–280. https://doi.org/10.1016/j.pepi.2006.01.010.

Bastow, I., Pilidou, S., Kendall, J.-M., Stuart, G., 2010. Melt-induced seismic anisotropy and magma assisted rifting in Ethiopia: evidence from surface waves. Geochem. Geosyst. 11, Q0AB05. https://doi.org/10.1029/2010GC003036.

Becker, G., Knapmeyer-Endrun, B., 2018. Crustal thickness across the Trans-European Suture Zone from ambient noise autocorrelations. Geophys. J. Int. 212 (2), 1237–1254. https://doi.org/10.1093/gji/ggx485.

Behr, H.-J., Engel, W., Franke, W., Giese, P., Weber, K., 1984. The Variscan Belt in Central Europe: Main structures, geodynamic implications, open questions. Tectonophysics 109 (1), 15–40. https://doi.org/10.1016/0040-1951(84)90168-9.

Bensen, G., Ritzwoller, M., Barmin, M., Levshin, A.L., Lin, F., Moschetti, M., Shapiro, N., Yang, Y., 2007. Processing seismic ambient noise data to obtain reliable broad-band surface wave dispersion measurements. Geophys. J. Int. 169 (3), 1239–1260. https://doi.org/10.1111/j.1365-246X.2007.03374.x.

Bijwaard, H., Spakman, W., 2000. Non-linear global P-wave tomography by iterated linearized inversion. Geophys. J. Int. 141 (1), 71–82. https://doi.org/10.1046/j.1365-246X.2000.00053.x.

Bodin, T., Sambridge, M., Tkalčić, H., Arroucau, P., Gallagher, K., Rawlinson, N., 2012. Transdimensional inversion of receiver functions and surface wave dispersion. J. Geophys. Res. Solid Earth 117 (B2). http://dx.doi.org/10.1029/2011JB008560

Bogdanova, S., Pashkevich, I., Gorbatschev, R., Orlyuk, M., 1996. Riphean rifting and major Palaeoproterozoic crustal boundaries in the basement of the East European Craton: geology and geophysics. Tectonophysics 268 (1–4), 1–21. https://doi.org/10.1016/S0040-1951(96)00232-6.

Bogdanova, S., Gorbatschev, R., Grad, M., Janik, T., Guterch, A., Kozlovskaya, E., Motuza, G., Skridlaite, G., Starostenko, V., Taran, L., et al., 2006. EUROBRIDGE: new insight into the geodynamic evolution of the East European Craton. Geol. Soc. Lond. Mem. 32 (1), 599–625. https://doi.org/10.1144/GSL.MEM.2006.032.01.36.

Bogdanova, S., Bingen, B., Gorbatschev, R., Kheraskova, T., Kozlov, V., Puchkov, V., Volozh, Y.A., 2008. The East European Craton (Baltica) before and during the assembly of Rodinia. Precambr. Res. 160 (1–2), 23–45. https://doi.org/10.1016/j.precamres.2007.04.024.

Bogdanova, S., Gorbatschev, R., Skridlaite, G., Soesoo, A., Taran, L., Kurlovich, D., 2015. Trans-Baltic Palaeoproterozoic correlations towards the reconstruction of supercontinent Columbia/Nuna. Precambr. Res. 259, 5–33. https://doi.org/10.1016/j.precamres.2014.11.023.

Boness, N.L., Zoback, M.D., 2006. Mapping stress and structurally controlled crustal shear velocity anisotropy in California. Geology 34 (10), 825–828. https://doi.org/10.1130/G22309.1.

Borleanu, F., Petrescu, L., Enescu, B., Popa, M., Radulian, M., 2021. The missing craton edge: Crustal structure of the East European Craton beneath the Carpathian Orogen revealed by double-difference tomography. Global Planet. Change 197 103, 390. https://doi.org/10.1016/j.gloplacha.2020.103390.

Borleanu, F., Petrescu, L., Seghedi, I., Thomas, C., De Siena, L., 2023. The seismic attenuation signature of collisional orogens and sedimentary basins within the Carpathian Orogen. Global Planet. Change 223 (104), 093. https://doi.org/10.1016/j.gloplacha.2023.104093.

Calvert, A., Sawyer, E., Davis, W., Ludden, J., 1995. Archaean subduction inferred from seismic images of a mantle suture in the Superior Province. Nature 375, 670–674. https://doi.org/10.1038/375670a0.

Chang, S.-J., Van Der Lee, S., Flanagan, M.P., Bedle, H., Marone, F., Matzel, E.M., Pasyanos, M.E., Rodgers, A.J., Romanowicz, B., Schmid, C., 2010. Joint inversion for three-dimensional S velocity mantle structure along the Tethyan margin, Journal of Geophysical Research: Solid. Earth 115 (B8). https://doi.org/10.1029/2009JB007204.

Chen, Y., Saygin, E., Kennett, B., Qashqai, M.T., Hauser, J., Lumley, D., Sandiford, M., 2023. Next-generation seismic model of the Australian crust from synchronous and asynchronous ambient noise imaging. Nature Communications 14 (1), 1192. https://doi.org/10.1038/s41467-023-36514-z.

Claesson, S., Bibikova, E., Bogdanova, S., Skobelev, V., 2006. Archaean terranes, Palaeoproterozoic reworking and accretion in the Ukrainian shield, East European Craton, Geological Society, London. Memoirs 32 (1), 645–654.

Crampin, S., 1994. The fracture criticality of crustal rocks. Geophys. J. Int. 118, 428–438.

Crampin, S., Peacock, S., 2008. A review of the current understanding of seismic shear-wave splitting in the Earth's crust and common fallacies in interpretation. Wave Motion 45 (6), 675–722. https://doi.org/10.1016/j.wavemoti.2008.01.003.

Curtis, A., Gerstoft, P., Sato, H., Snieder, R., Wapenaar, K., 2006. Seismic interferometry— Turning noise into signal. Lead. Edge 25 (9), 1082–1092.

Dando, B., Stuart, G., Houseman, G., HegedÅNus, E., BrÅNuckl, E., RadovanoviÅLc, S., 2011. Teleseismic tomography of the mantle in the Carpathian-Pannonian region of central Europe. Geophys. J. Int. 186 (1), 11–31. https://doi.org/10.1111/j.1365-246X.2011.04998.x.

Darbyshire, F., Lebedev, S., 2009. Rayleigh wave phase-velocity heterogeneity and multilayered azimuthal anisotropy of the Superior Craton, Ontario. Geophys. J. Int. 176 (1), 215–234. https://doi.org/10.1111/j.1365-246X.2008.03982.x.

Deschamps, F., Lebedev, S., Meier, T., Trampert, J., 2008. Azimuthal anisotropy of Rayleigh-wave phase velocities in the east-central United States. Geophys. J. Int. 173 (3), 827–843. https://doi.org/10.1111/j.1365-246X.2008.03751.x.

Bracco Gartner, A. J., McKenzie, D. (2020), Estimates of the temperature and melting conditions of the Carpathian-Pannonian upper mantle from volcanism and seismology, Geochemistry, Geophysics, Geosystems, 21 (10), e2020GC009,334. http://dx.doi.org/10.1029/2020GC009334

Dreiling, J., Tilmann, F., 2019. BayHunter-McMC transdimensional Bayesian inversion of receiver functions and surface wave dispersion, http://dx.doi.org/10.5880/GFZ.2.4.2019.001.

Durrheim, R., Mooney, W., 1991. Archean and Proterozoic Crustal Evolution: Evidence from Crustal Seismology. Geology 19 (6), 606–609. http://dx.doi.org/10.1130/0091-7613(1991)019<0606:AAPCEE>2.3.CO;2

EUROBRIDGE Seismic Working Group, 1999. Seismic velocity structure across the Fennoscandia-Sarmatia suture of the East European Craton beneath the EUROBRIDGE profile through Lithuania and Belarus. Tectonophysics 314 (1–3), 193–217. https://doi.org/10.1016/S0040-1951(99)00244-9.

Fouch, M.J., Rondenay, S., 2006. Seismic anisotropy beneath stable continental interiors. Phys. Earth Planet. Int. 158 (2), 292–320. https://doi.org/10.1016/j.pepi.2006.03.024.

Fry, B., Deschamps, F., Kissling, E., Stehly, L., Giardini, D., 2010. Layered azimuthal anisotropy of Rayleigh wave phase velocities in the European Alpine lithosphere inferred from ambient noise. Earth Planet. Sci. Lett. 297 (1–2), 95–102. https://doi.org/10.1016/j.epsl.2010.06.008.

Gee, D., Stephenson, R., 2006. European lithosphere — an introduction. European Lithosphere Dynamics, vol. 32. Geological Society of London, Memoir, pp. 1–9.

Gerya, T., 2014. Precambrian geodynamics: concepts and models. Gondw. Res. 25 (2), 442–463. https://doi.org/10.1016/j.gr.2012.11.008.

Gorbatschev, R., Bogdanova, S., 1993. Frontiers in the Baltic shield. Precambr. Res. 64 (1–4), 3–21. https://doi.org/10.1016/0301-9268(93)90066-B.

Grad, M., Keller, G., Thybo, H., Guterch, A., Group, P.W., et al., 2002. Lower lithospheric structure beneath the Trans-European Suture Zone from POLONAISE'97 seismic profiles. Tectonophysics 360 (1–4), 153–168. https://doi.org/10.1016/S0040-1951(02)00350-5.

Grad, M., Gryn, D., Guterch, A., Janik, T., Keller, R., Lang, R., Lyngsie, S., Omelchenko, V., Starostenko, V., Stephenson, R., et al., 2003. DOBREfraction'99"—velocity model of the crust and upper mantle beneath the Donbas Foldbelt (East Ukraine). Tectonophysics 371 (1–4), 81–110. https://doi.org/10.1016/S0040-1951(03)00211-7.

Grad, M., Guterch, A., Keller, G.R., Janik, T., Hegedüs, E., Vozár, J., Ślaczka, A., Tiira, T., Yliniemi, J., 2006. Lithospheric structure beneath trans-Carpathian transect from Precambrian platform to Pannonian basin: CELEBRATION 2000 seismic profile CEL05. J. Geophys. Res. Solid Earth 111 (B3). http://dx.doi.org/10.1029/2005JB003647

Guterch, A., Grad, M., Thybo, H., Keller, G., Group, P.W., et al., 1999. POLONAISE'97— an international seismic experiment between Precambrian and Variscan Europe in Poland. Tectonophysics 314 (1–3), 101–121. https://doi.org/10.1016/S0040-1951(99)00239-5.

Hamilton, W.B., 2011. Plate tectonics began in Neoproterozoic time, and plumes from deep mantle have never operated. Lithos 123 (1–4), 1–20. https://doi.org/10.1016/j.lithos.2010.12.007.

Hauser, F., Raileanu, V., Fielitz, W., Bala, A., Prodehl, C., Polonic, G., Schulze, A., 2001. VRANCEA99—the crustal structure beneath the southeastern Carpathians and the Moesian Platform from a seismic refraction profile in Romania. Tectonophysics 340 (3–4), 233–256. https://doi.org/10.1016/S0040-1951(01)00195-0.

Hauser, F., Raileanu, V., Fielitz, W., Dinu, C., Landes, M., Bala, A., Prodehl, C., 2007. Seismic crustal structure between the Transylvanian Basin and the Black Sea. Romania, Tectonophysics 430 (1–4), 1–25. https://doi.org/10.1016/j.tecto.2006.10.005.

Hippolyte, J.-C., Badescu, D., Constantin, P., 1999. Evolution of the transport direction of the Carpathian belt during its collision with the east European Platform. Tectonics 18 (6), 1120–1138. https://doi.org/10.1029/1999TC900027.

Hippolyte, J.-C., Murovskaya, A., Volfman, Y., Yegorova, T., Gintov, O., Kaymakci, N., Sangu, E., 2018. Age and geodynamic evolution of the Black Sea Basin: Tectonic evidences of rifting in Crimea. Mar. Pet. Geol. 93, 298–314. https://doi.org/10.1016/j.marpetgeo.2018.03.009.

Horváth, F., Bada, G., Szafián, P., Tari, G., Ádám, A., Cloetingh, S., 2006. Formation and deformation of the Pannonian Basin: constraints from observational data. Geol. Soc. Lond. Spec. Pub. 32 (1), 191–206. https://doi.org/10.1144/GSL.MEM.2006.032.01.11.

Hrubcová, P., ÅLSroda, P., Grad, M., Geissler, W., Guterch, A., Vozár, J., Hegedüs, E., 2010. From the Variscan to the Alpine Orogeny: crustal structure of the Bohemian Massif and the Western Carpathians in the light of the SUDETES 2003 seismic data. Geophys. J. Int. 183 (2), 611–633. https://doi.org/10.1111/j.1365-246X.2010.04766.

Huismans, R.S., Bertotti, G., 2002. The Transylvanian basin, transfer zone between coeval extending and contracting regions: Inferences on the relative importance of slab pull and rift push in arc–back arc systems. Tectonics 21 (2), 2–11. https://doi.org/10.1029/2001TC900026.

Jain, C., Rozel, A.B., Tackley, P.J., Sanan, P., Gerya, T., 2019. Growing primordial continental crust self-consistently in global mantle convection models. Gondw. Res. 73, 96–122. https://doi.org/10.1016/j.gr.2019.03.015.

Kalmár, D., Hetényi, G., Balázs, A., Bondár, I., Group, A.W., 2021. Crustal Thinning From Orogen to Back-Arc Basin: The Structure of the Pannonian Basin Region Revealed by P-to-S Converted Seismic Waves. J. Geophys. Res.: Solid Earth 126 (7). https://doi.org/10.1029/2020JB021,309.

Kalmár, D., Petrescu, L., Stipčević, J., Balázs, A., Kovács, I.J., AlpArray, PACASE Working Groups, 2023. Lithospheric structure of the circum-Pannonian region imaged by S-to-P receiver functions. Geochem., Geophys. 24, e2023GC010937. https://doi.org/10.1029/2023GC010937.

Karato, S.-I., Jung, H., Katayama, I., Skemer, P., 2008. Geodynamic significance of seismic anisotropy of the upper mantle: new insights from laboratory studies. Annu. Rev. Earth Planet. Sci. 36, 59–95. https://doi.org/10.1146/annurev.earth.36.031207.124120.

Kästle, E., Molinari, I., Boschi, L., Kissling, E., Group, A.W., 2022. Azimuthal anisotropy from eikonal tomography: example from ambient-noise measurements in the AlpArray network. Geophys. J. Int. 229 (1), 151–170. https://doi.org/10.1093/gji/ggab453.

Kästle, E.D., Soomro, R., Weemstra, C., Boschi, L., Meier, T., 2016. Two-receiver measurements of phase velocity: cross-validation of ambient-noise and earthquake-based observations. Geophys. J. Int. 207 (3), 1493–1512. https://doi.org/10.1093/gji/ggw341.

Kendall, J.-M., Stuart, G., Ebinger, C., Bastow, I., Keir, D., 2005. Magma assisted rifting in Ethiopia. Nature 433, 146–148. https://doi.org/10.1038/nature03161.

Kern, H., 1990. Laboratory seismic measurements: an aid in the interpretation of seismic field data. Terra Nova 2 (6), 617–628. https://doi.org/10.1111/j.1365-3121.1990.tb00127.x.

Knapmeyer-Endrun, B., KrÅNuger, F., Legendre, C.P., Geissler, W.H., Group, P.W., et al., 2013. Tracing the influence of the Trans-European Suture Zone into the mantle transition zone. Earth Planetary Sci. Lett. 363, 73–87. https://doi.org/10.1016/j.epsl.2012.12.028.

Knapmeyer-Endrun, B., KrÅNuger, F., Group, T.P.W., 2014. Moho depth across the Trans- European Suture Zone from P-and S-receiver functions. Geophys. J. Int. 197 (2), 1048–1075. https://doi.org/10.1093/gji/ggu035.

Korenaga, J., 2013. Initiation and evolution of plate tectonics on Earth: theories and observations. Annu. Rev. Earth Planet. Sci. 41 (1), 117–151. https://doi.org/10.1146/annurev-earth-050212-124208.

Krzemińska, E., Poprawa, P., Pacześna, J., Krzemiński, L., 2022. From initiation to termination: The evolution of the Ediacaran Volyn large igneous province (SW East European Craton) constrained by comparative geochemistry of proximal tuffs versus lavas and zircon geochronology. Precambr. Res. 370 (106), 560. https://doi.org/10.1016/j.precamres.2022.106560.

Legendre, C.P., Deschamps, F., Zhao, L., Chen, Q.-F., 2015. Rayleigh-wave dispersion reveals crust-mantle decoupling beneath eastern Tibet. Sci. Rep. 5 (1), 1–7. https://doi.org/10.1038/srep16644.

Legendre, C., Meier, T., Lebedev, S., Friederich, W., Viereck-GÅNotte, L., 2012. A shear wave velocity model of the European upper mantle from automated inversion of seismic shear and surface waveforms. Geophys. J. Int. 191 (1), 282–304. https://doi.org/10.1111/j.1365- 246X.2012.05613.x.

Li, H., Bernardi, F., Michelini, A., 2010. Surface wave dispersion measurements from ambient seismic noise analysis in Italy. Geophys. J. Int. 180 (3), 1242–1252. https://doi.org/10.1111/j.1365-246X.2009.04476.x.

Long, M.D., Becker, T.W., 2010. Mantle dynamics and seismic anisotropy. Earth Planet. Sci. Lett. 297 (3), 341–354. https://doi.org/10.1016/j.epsl.2010.06.036.

Lu, Y., Stehly, L., Paul, A., Group, A.W., 2018. High-resolution surface wave tomography of the European crust and uppermost mantle from ambient seismic noise. Geophys. J. Int. 214 (2), 1136–1150. https://doi.org/10.1093/gji/ggy188.

Magrini, F., Lauro, S., Kästle, E., Boschi, L., 2022. Surface-wave tomography using SeisLib: a Python package for multiscale seismic imaging. Geophys. J. Int. 231 (2), 1011–1030. https://doi.org/10.1093/gji/ggac236.

Mainprice, D., Nicolas, A., 1989. Development of shape and lattice preferred orientations: application to the seismic anisotropy of the lower crust. J. Struct. Geol. 11, 175–189. https://doi.org/10.1016/0191-8141(89)90042-4.

Martin, M., Ritter, J., Group, C.W., 2005. High-resolution teleseismic body-wave tomography beneath SE Romania—I. Implications for three-dimensional versus one-dimensional crustal correction strategies with a new crustal velocity model. Geophys. J. Int. 162 (2), 448–460. https://doi.org/10.1111/j.1365-246X.2005.02661.x.

Meier, T., Soomro, R., Viereck, L., Lebedev, S., Behrmann, J., Weidle, C., Cristiano, L., Hanemann, R., 2016. Mesozoic and Cenozoic evolution of the Central European lithosphere. Tectonophysics 692, 58–73. https://doi.org/10.1016/j.tecto.2016.09.016.

Meissner, R., 1989. Rupture, creep, lamellae and crocodiles: happenings in the continental crust. Terra Nova 1 (1), 17–28. https://doi.org/10.1111/j.1365-3121.1989.tb00321.x.

Mints, M., 2018. A Neoarchean-Proterozoic supercontinent (~ 2.8–0.9 Ga): an alternative to the model of supercontinent cycles. In: Doklady Earth Sciences, 480. Springer, pp. 555–558. https://doi.org/10.1134/S1028334X18050045.

Mints, M., 2015. East European Craton: Early Precambrian History and 3D Models of Deep Crustal Structure., in TEvolution and major features of the Early Precambrian crust of the East European craton,, vol. 510, edited by M. Mints, K. Dokukina, A. Konilov, I. Philippova, V. Zlobin, P. Babayants, E. Belousova, Y. Blokh, M. Bogina, W. Bush, P. Dokukin, T. Kaulina, L. Natapov, V. Piip, V. Stupak, A. Suleimanov, A. Trusov, K. Van, and N. Zamozhniaya, pp. 333—-354, Geological Society of America Special Papers, doi: 10.1130/2015.2510(17).

Nelskamp, S., 2017. Geological resource analysis of shale gas and shale oil in Europe, Report T4b of the EUOGA Study (EU Unconventional Oil and Gas Assessment) commissioned by JRC-IET.

Nicolas, A., Christensen, N., 1987. Formation of anisotropy in upper mantle peridotites-A review, Composition, structure and dynamics of the lithosphere–asthenosphere system 16, 111–123. https://doi.org/10.1029/GD016p0111.

Nikishin, A., Ziegler, P., Stephenson, R., Cloetingh, S., Furne, A., Fokin, P., Ershov, A., Bolotov, S., Korotaev, M., Alekseev, A., et al., 1996. Late Precambrian to Triassic history of the East European Craton: dynamics of sedimentary basin evolution. Tectonophysics 268 (1–4), 23–63. https://doi.org/10.1016/S0040-1951(96)00228-4.

Nita, B., Maurya, S., Montagner, J.-P., 2016. Anisotropic tomography of the European lithospheric structure from surface wave studies. Geochem. Geophys. Geosyst. 17 (6), 2015–2033. https://doi.org/10.1002/2015GC006243.

Oczlon, M.S., Seghedi, A., Carrigan, C.W., 2007. Avalonian and Baltican terranes in the Moesian Platform (southern Europe, Romania, and Bulgaria) in the context of Caledonian terranes along the southwestern margin of the East European craton. Geological Society of America - Special Papers 423, 375. https://doi.org/10.1130/2007.2423(18).

Paige, C.C., Saunders, M.A., 1982. LSQR: An algorithm for sparse linear equations and sparse least squares. ACM Transactions on Mathematical Software (TOMS) 8 (1), 43–71. https://doi.org/10.1145/355993.356000.

Petrescu, L., Bastow, I., Darbyshire, F., Gilligan, A., Bodin, T., Menke, W., Levin, V., 2016. Three billion years of crustal evolution in eastern Canada: Constraints from receiver functions. J. Geophys. Res. https://doi.org/10.1002/2015JB012348.

Petrescu, L., Darbyshire, F., Bastow, I., Totten, E., Gilligan, A., 2017. Seismic anisotropy of Precambrian lithosphere: Insights from Rayleigh wave tomography of the eastern Superior Craton. J. Geophys. Res. 122 (5), 3754–3775. https://doi.org/10.1002/2016JB013599.

Petrescu, L., Stuart, G., Tataru, D., Grecu, B., 2019. Crustal structure of the Carpathian Orogen in Romania from receiver functions and ambient noise tomography: how craton collision, subduction and detachment affect the crust. Geophys. J. Int. https://doi.org/10.1093/gji/ggz140.

Petrescu, L., Borleanu, F., Placinta, A.O., 2022. Seismic structure of a Tethyan back-arc: Transdimensional ambient noise tomography of the Black Sea lithosphere. Phys. Earth Planet. Inter. 325 (106), 854. https://doi.org/10.1016/j.pepi.2022.106854.

Pharaoh, T.C., 1999. Palaeozoic terranes and their lithospheric boundaries within the Trans- European Suture Zone (TESZ): a review. Tectonophysics 314 (1–3), 17–41. https://doi.org/10.1016/S0040-1951(99)00235-8.

Pharaoh, T., Winchester, J., Verniers, J., Lassen, A., Seghedi, A., 2006. The western accretionary margin of the East European Craton: an overview. Geological Society of London - Memoirs 32, 291. https://doi.org/10.1144/GSL.MEM.2006.032.01.17.

Plomerová, J., Vecsey, L., Babuška, V., Group, L.W., et al., 2011. Domains of Archean mantle lithosphere deciphered by seismic anisotropy–inferences from the LAPNET array in northern Fennoscandia. Solid Earth 2 (2), 303–313. https://doi.org/10.5194/se-2-303-2011.

Poprawa, P., 2019. Geological setting and Ediacaran–Palaeozoic evolution of the western slope of the East European Craton and adjacent regions. Annales Societatis Geologorum Poloniae 89 (4), 347–380. https://doi.org/10.14241/asgp.2019.23.

Posgay, K., Albu, I., Petrovics, I., RÅLaner, G., 1981. Character of the Earth's crust and upper mantle on the basis of seismic reflection measurements in Hungary. Earth Evol. Sci 1 (3/4), 272–279.

Radulian, M., Bălă, A., Ardeleanu, L., Toma-Dănilă, D., Petrescu, L., Popescu, E., 2019. Revised catalogue of earthquake mechanisms for the events occurred in Romania until the end of twentieth century: REFMC. Acta Geod. Geophys. 54 (1), 3–18. https://doi.org/10.1007/s40328- 018-0243-y.

Ratschbacher, L., Frisch, W., Linzer, H.-G., Merle, O., 1991. Lateral extrusion in the Eastern Alps, part 2: structural analysis. Tectonics 10 (2), 257–271. https://doi.org/10.1029/90TC02623.

Ren, Y., Stuart, G., Houseman, G., Dando, B., Ionescu, C., Hegedüs, E., Radovanović, S., Shen, Y., SCP Working Group, et al., 2012. Upper mantle structures beneath the Carpathian-Pannonian region: Implications for the geodynamics of continental collision. Earth Planet Sci. Lett. 349, 139–152. https://doi.org/10.1016/j.epsl.2012.06.037.

Ren, Y., Grecu, B., Stuart, G., Houseman, G., Hegedüs, E., Group, S.C.P.W., 2013. Crustal structure of the Carpathian-Pannonian region from ambient noise tomography. Geophys. J. Int. 195 (2), 1351–1369. https://doi.org/10.1093/gji/ggt316.

Ribe, N.M., 1992. On the relation between seismic anisotropy and finite strain. J. Geophys. Res. Solid Earth 97 (B6),, 8737–8747. https://doi.org/10.1029/92JB00551.

Ritzwoller, M.H., Levshin, A.L., 1998. Eurasian surface wave tomography: Group velocities. J. Geophys. Res. Solid Earth 103 (B3), 4839–4878. http://dx.doi.org/10.1029/97JB02622

Royden, L.H., 1988. Late Cenozoic tectonics of the Pannonian Basin system. AAPG Mem. 45, 27–48.

Rudnick, R.L., Fountain, D.M., 1995. Nature and composition of the continental crust: a lower crustal perspective. Rev. Geophys. 33 (3), 267–309. https://doi.org/10.1029/95RG01302.

Saintot, A., Stephenson, R.A., Stovba, S., Brunet, M.-F., Yegorova, T., Starostenko, V., 2006. The evolution of the southern margin of Eastern Europe (Eastern European and Scythian platforms) from the latest Precambrian-Early Palaeozoic to the Early Cretaceous. Geol. Soc. Lond. Mem. 32 (1), 481–505. https://doi.org/10.1144/GSL.MEM.2006.032.01.30.

Schaeffer, A., Lebedev, S., 2013. Global shear speed structure of the upper mantle and transition zone. Geophys. J. Int. 194 (1), 417–449. https://doi.org/10.1093/gji/ggt095.

Schivardi, R., Morelli, A., 2011. EPmantle: a 3-D transversely isotropic model of the upper mantle under the European Plate. Geophys. J. Int. 185 (1), 469–484. https://doi.org/10.1111/j.1365-246X.2011.04953.x.

Schmid, S.M., Bernoulli, D., Fügenschuh, B., Maţenco, L., Schefer, S., Schuster, R., Tischler, M., Ustaszewski, K., 2008. The Alpine-Carpathian-Dinaridic orogenic system: correlation and evolution of tectonic units. Swiss J. Geosci. 101 (1), 139–183. https://doi.org/10.1007/s00015-008- 1247-3.

Seghedi, I., Downes, H., Vaselli, O., Szakács, A., Balogh, K., Pécskay, Z., 2004. Postcollisional Tertiary-Quaternary mafic alkalic magmatism in the Carpathian-Pannonian region: a review. Tectonophysics 393 (1–4), 43–62. https://doi.org/10.1016/j.tecto.2004.07.051.

Shen, W., Ritzwoller, M.H., Kang, D., Kim, Y., Lin, F.-C., Ning, J., Wang, W., Zheng, Y., Zhou, L., 2016. A seismic reference model for the crust and uppermost mantle beneath China from surface wave dispersion. Geophys. J. Int. 206 (2), 954–979. https://doi.org/10.1093/gji/ggw175.

Shumlyanskyy, L., Andreasson, P.-G., Buchan, K.L., Ernst, R.E., 2007. The Volynian flood basalt province and coeval (Ediacaran) magmatism in Baltoscandia and Laurentia. Mineralogical Journal (Ukraine) 29 (4), 47–55.

Shumlyanskyy, L., Mitrokhin, O., BillstrÅNom, K., Ernst, R., Vishnevska, E., Tsymbal, S., Cuney, M., Soesoo, A., 2016. The ca. 1.8 Ga mantle plume related magmatism of the central part of the Ukrainian shield. GFF 138 (1), 86–101. https://doi.org/10.1080/11035897.2015.1067253.

Snyder, D., 2002. Lithospheric growth at margins of cratons. Tectonophysics 355 (1), 7–22. https://doi.org/10.1016/S0040-1951(02)00131-2.

Soomro, R., Weidle, C., Cristiano, L., Lebedev, S., Meier, T., Group, P.W., 2016. Phase velocities of Rayleigh and Love waves in central and northern Europe from automated, broadband, interstation measurements. Geophys. J. Int. 204 (1), 517–534. https://doi.org/10.1093/gji/ggv462.

Środa, P., Czuba, W., Grad, M., Guterch, A., Tokarski, A., Janik, T., Rauch, M., Keller, G., Hegedüs, E., Vozár, J., et al., 2006. Crustal and upper mantle structure of the Western Carpathians from CELEBRATION 2000 profiles CEL01 and CEL04: seismic models and geological implications. Geophys. J. Int. 167 (2), 737–760.

Starostenko, V., Janik, T., Kolomiyets, K., Czuba, W., Środa, P., Grad, M., Kovács, I., Stephenson, R., Lysynchuk, D., Thybo, H., et al., 2013. Seismic velocity model of the crust and upper mantle along profile pancake across the carpathians between the pannonian basin and the east european craton. Tectonophysics 608, 1049–1072. https://doi.org/10.1016/j.tecto.2013.07.008.

Starostenko, V., Janik, T., Gintov, O., Lysynchuk, D., ÅLSroda, P., Czuba, W., Kolomiyets, E., Aleksandrowski, P., Omelchenko, V., Komminaho, K., et al., 2017. Crustal and upper mantle velocity model along the DOBRE-4 profile from North Dobruja to the central region of the Ukrainian Shield: 1. seismic data. Izv. Phys. Solid Earth 53 (2), 193–204.

Starostenko, V., Janik, T., Mocanu, V., Stephenson, R., Yegorova, T., Amashukeli, T., Czuba, W., Środa, P., Murovskaya, A., Kolomiyets, K., et al., 2020. RomUkrSeis: Seismic model of the crust and upper mantle across the Eastern Carpathians-From the Apuseni Mountains to the Ukrainian Shield. Tectonophysics 794 (228), 620. https://doi.org/10.1016/j.tecto.2020.228620.

Stephenson, R., Yegorova, T., Brunet, M.-F., Stovba, S., Wilson, M., Starostenko, V., Saintot, A., Kusznir, N., 2006. Late Palaeozoic intra-and pericratonic basins on the East European Craton and its margins. Geol. Soc. Lond. Mem. 32 (1), 463–479. https://doi.org/10.1144/GSL.MEM.2006.032.01.29.

Stephenson, R., Yegorova, T., Stovba, S., 2021. An investigation of how intracratonic rifting is "seeded": Case study of the Late Devonian Dniepr-Donets Basin rift within the East European Craton. Precambr. Res. 362 (106), 305. https://doi.org/10.1016/j.precamres.2021.106305.

Stern, R., 2005. Evidence from ophiolites, blueschists, and ultrahigh-pressure metamorphic terranes that the modern episode of subduction tectonics began in Neoproterozoic time. Geology 33 (7), 557–560. https://doi.org/10.1130/G21365.1.

Szanyi, G., Gráczer, Z., Balázs, B., Kovács, I.J., Group, A.W., et al., 2021. The transition zone between the Eastern Alps and the Pannonian basin imaged by ambient noise tomography. Tectonophysics 805 (228), 770. https://doi.org/10.1016/j.tecto.2021.228770.

Thybo, H., Janik, T., Omelchenko, V., Grad, M., Garetsky, R., Belinsky, A., Karatayev, G., Zlotski, G., Knudsen, M., Sand, R., et al., 2003. Upper lithospheric seismic velocity structure across the Pripyat Trough and the Ukrainian Shield along the EUROBRIDGE'97 profile. Tectonophysics 371 (1–4), 41–79. https://doi.org/10.1016/S0040-1951(03)00200-2.

Ustaszewski, K., Schmid, S.M., Fånugenschuh, B., Tischler, M., Kissling, E., Spakman, W., 2008. A map-view restoration of the Alpine-Carpathian-Dinaridic system for the Early Miocene. Swiss J. Geosci. 101 (1), 273–294. https://doi.org/10.1007/s00015-008-1288-7.

Van Kranendonk, M.J., Collins, W., Hickman, A., Pawley, M.J., 2004. Critical tests of vertical vs. horizontal tectonic models for the Archaean East Pilbara granite–greenstone terrane, Pilbara craton, Western Australia. Precambr. Res. 131 (3–4), 173–211. https://doi.org/10.1016/j.precamres.2003.12.015.

Wang, Z., Dahlen, F., 1995. Spherical-spline parameterization of three-dimensional Earth models. Geophys. Res. Lett. 22 (22), 3099–3102. https://doi.org/10.1029/95GL03080.

Wessel, P., Smith, W.H., 1998. New, improved version of Generic Mapping Tools released. Eos. Transactions American Geophysical Union 79 (47), 579. https://doi.org/10.1029/98EO00426.

Wilde-Piorko, M., Geissler, W., Plomerová, J., Grad, M., Babuska, V., Brückl, E., Cyziene, J., Czuba, W., England, R., Gaczyski, E., et al., 2008. PASSEQ 2006–2008: passive seismic experiment in Trans-European Suture Zone. Stud. Geophys. Geod. 52 (3), 439. https://doi.org/10.1007/s11200-008-0030-2.

Wilson, M., Lyashkevich, Z.M., 1996. Magmatism and the geodynamics of rifting of the Pripyat-Dnieper-Donets rift. East European Platform. Tectonophysics 268 (1–4), 65–81. https://doi.org/10.1016/S0040-1951(96)00234-X.

Wüstefeld, A., Bokelmann, G., Barruol, S., 2010. Evidence for ancient lithospheric deformation in the East European Craton based on mantle seismic anisotropy and crustal magnetics. Tectonophysics 481 (1–4), 16–28. https://doi.org/10.1016/j.tecto.2009.01.010.

Yang, Y., Ritzwoller, M.H., Levshin, A.L., Shapiro, N.M., 2007. Ambient noise Rayleigh wave tomography across Europe. Geophys. J. Int. 168 (1), 259–274. https://doi.org/10.1111/j.1365-246X.2006.03203.x.

Yang, Y., Liu, C., Langston, C.A., 2020. Processing seismic ambient noise data with the continuous wavelet transform to obtain reliable empirical Green's functions. Geophys. J. Int. 222 (2), 1224–1235. https://doi.org/10.1093/gji/ggaa243.

Yegorova, T., Starostenko, V., Kozlenko, V., Yliniemi, J., 2004. Lithosphere structure of the Ukrainian Shield and Pripyat Trough in the region of EUROBRIDGE-97 (Ukraine and Belarus) from gravity modelling. Tectonophysics 381 (1–4), 29–59. https://doi.org/10.1016/j.tecto.2002.06.003.

Yliniemi, J., Tiira, T., Luosto, U., Komminaho, K., Giese, R., Motuza, G., Nasedkin, V., Jacyna, J., Seckus, R., Grad, M., et al., 2001. EUROBRIDGE'95: deep seismic profiling within the East European Craton. Tectonophysics 339 (1–2), 153–175. https://doi.org/10.1016/S0040-1951(01)00037-3.

Yuan, H., 2015. Secular change in Archaean crust formation recorded in Western Australia. Nat. Geosci. 8 (10), 808–813. https://doi.org/10.1038/ngeo2521.

Zegers, T., Van Keken, P., 2001. Middle Archean continent formation by crustal delamination. Geology 29 (12), 1083–1086. https://doi.org/10.1130/0091-7613(2001)029.1083:MACFBC.2.0.CO;2.

Zhu, H., Tromp, J., 2013. Mapping tectonic deformation in the crust and upper mantle beneath Europe and the North Atlantic Ocean. Science 341 (6148), 871–875. https://doi.org/10.1126/science.1241335.

Zhu, H., Bozdag, E., Peter, D., Tromp, J., 2012. Structure of the European upper mantle revealed by adjoint tomography. Nat. Geosci. 5 (7), 493–498. https://doi.org/10.1038/ngeo1501.

Zhu, H., Bozdag, E., Tromp, J., 2015. Seismic structure of the European upper mantle based on adjoint tomography. Geophys. J. Int. 201 (1), 18–52. https://doi.org/10.1093/gji/ggu492.

Zielhuis, A., Nolet, G., 1994. Deep seismic expression of an ancient plate boundary in Europe. Science 265 (5168), 79–81. https://doi.org/10.1126/science.265.5168.79.